

Computing hydrodynamic interactions in confined doubly-periodic geometries in linear time

Aref Hashemi,* Raul P. Pelaez, Sachin Natesh, Ondrej Maxian,

Brennan Sprinkle, Zecheng Gan, and Aleksandar Donev[†]

Courant Institute, New York University, New York, NY, United States

We develop a linearly-scaling variant of the Force Coupling Method [K. Yeo and M. R. Maxey, *J. Fluid Mech.* 649, 205–231 (2010)] for computing hydrodynamic interactions among particles confined to a doubly-periodic geometry with either a single bottom wall or two walls (slit channel) in the aperiodic direction. Our spectrally-accurate Stokes solver uses the Fast Fourier Transform (FFT) in the periodic xy plane and Chebyshev polynomials in the aperiodic z direction normal to the wall(s). We decompose the problem into two subproblems. The first is a doubly-periodic system in the presence of particles (source terms) with free-space boundary conditions in the z direction, which we solve by borrowing ideas from a recent method for rapid evaluation of electrostatic interactions in doubly-periodic geometries [O. Maxian, R. P. Pelaez, L. Greengard and A. Donev, *J. Chem. Phys.* 154, 204107 (2021)]. The second is a correction subproblem to impose the boundary conditions on the wall(s). Instead of the traditional Gaussian kernel, we use the exponential of a semicircle kernel to model the source terms (body force) due to the presence of particles, and provide optimum values for the kernel parameters that ensure a given hydrodynamic radius with at least two digits of accuracy and rotational and translational invariance. The computation time of our solver, which is implemented in graphical processing units, scales linearly with the number of particles, and allows computations with about a million particles in less than a second for a sedimented layer of colloidal microrollers.

I. INTRODUCTION

The development of more efficient, accurate, and scalable methods for suspensions of rigid and flexible particles in Stokes flow remains a key challenge in soft condensed matter physics and chemical engineering. In addition to the long-ranged nature of hydrodynamic interactions, the inclusion of Brownian motion and the presence of confining boundaries pose particular difficulties. While confining boundaries partially screen the hydrodynamic interactions, they continue to decay algebraically rather than exponentially [1], and must be captured to resolve particle dynamics.

A key component of all computational methods for Stokes flow is the efficient evaluation of the action of the singular or regularized Green’s function for Stokes flow among a large number of particles. Specifically, given forces (and sometimes also torques) on many *source points*, the goal is to compute the resulting (linear and sometimes also angular) velocities on many *target points*, usually the same as the source points. While boundary integral methods typically use the singular Green’s function, most computational methods used for large-scale suspensions are based on a regularized Green’s function. There are three popular regularizations: the Rotne-Prager-Yamakawa (RPY) [2, 3] tensor, regularized Stokeslets [4], and the Force Coupling Method (FCM) kernel [5–9]. Both the RPY and FCM kernels regularize (smooth) the singularity at both the source and target; this is crucial to maintain the symmetric positive definite (SPD) nature of the hydrodynamic mobility matrix, as is necessary for Brownian Dynamics methods.

In this paper we develop a fast method for Stokes suspensions in *doubly periodic* geometries with one or two confining walls in the aperiodic direction. Our method is closely related to the Force Coupling Method of Yeo and Maxey [7], but with several important differences that increase both the flexibility and the efficiency of the approach. In brief, we employ a non-Gaussian envelope function [10] that allows accurate computations with many fewer grid cells per particles, as in immersed boundary methods [11], and also develop a novel spectral Stokes solver based on recent work by some of us on fast methods for electrostatics in doubly-periodic geometries [12].

To leading order, the hydrodynamic interaction between two spherical particles or *blobs* of radius a at positions $\mathbf{r}^{(1)}$ and $\mathbf{r}^{(2)}$ can be captured by a 3×3 mobility tensor that gives the velocity of one of the particles for a given force acting on the other. This hydrodynamic mobility tensor can be approximated in the far field as

$$\mathcal{R}(\mathbf{r}^{(1)}, \mathbf{r}^{(2)}) = \int \delta_a(\mathbf{r}^{(1)} - \mathbf{r}') \mathbb{G}(\mathbf{r}', \mathbf{r}'') \delta_a(\mathbf{r}^{(2)} - \mathbf{r}'') d\mathbf{r}' d\mathbf{r}'', \quad (1)$$

* aref@cims.nyu.edu

† corresponding author; donev@courant.nyu.edu

where \mathbb{G} is the Green's function for Stokes flow with the specified boundary conditions. Here $\delta_a(\mathbf{r})$ is a regularized “delta function” or *envelope function* [5] that is typically radially-symmetric, $\delta_a(\mathbf{r}) \equiv \delta_a(r)$, when the particles are sufficiently far from boundaries. It is important to point out that the blobs do not have to represent actual physical spherical colloids; one can build physical particles as a collection of blobs, including non-spherical rigid (passive or active) particles [13–17] we have termed *rigid multiblobs*, or flexible particles such as semiflexible fibers [18, 19]. If the blobs represent actual spherical colloids, additional near-field lubrication corrections can be added to improve upon the far-field accuracy [9, 14, 20, 21]; this requires including torques in addition to forces, as we do in the body of this paper.

Regardless of the context, a key task is to evaluate for N blobs their far-field velocity from the applied forces \mathbf{F} through the action of the *mobility matrix* \mathbf{M} , $\mathbf{U} = \mathbf{M}\mathbf{F}$,

$$\forall i : \quad \mathbf{U}^{(i)} = \sum_{j=1}^N \mathcal{R}(\mathbf{r}^{(i)}, \mathbf{r}^{(j)}) \mathbf{F}^{(j)} \quad (2)$$

in time linear in the number of blobs N . Note that the form of (1) guarantees that the mobility matrix is SPD by construction since \mathbb{G} is an SPD kernel, and the regularization is applied both at the source and the target.

The specific choice of δ_a as a delta function on the surface of a sphere of radius a , $\delta_a(\mathbf{r}) = (4\pi a^2)^{-1} \delta(r - a)$, results in the widely-used Rotne-Prager-Yamakawa (RPY) tensor [22–24]. When the kernels do not overlap the boundaries, one can transform (1) into a form employing the Faxen differential operator,

$$\mathcal{R}(\mathbf{r}^{(1)}, \mathbf{r}^{(2)}) \approx \left(\mathbf{I} + \frac{a^2}{6} \nabla_{\mathbf{r}'}^2 \right) \left(\mathbf{I} + \frac{a^2}{6} \nabla_{\mathbf{r}''}^2 \right) \mathbb{G}(\mathbf{r}', \mathbf{r}'') \Big|_{\mathbf{r}'' = \mathbf{r}^{(2)}}. \quad (3)$$

This analytical simplification allows for explicit evaluation of the RPY kernel, not just in an unbounded domain but also in a half-space above a no-slip wall [22], because for a single no-slip boundary there is a relatively simple image construction for \mathbb{G} due to Blake [25]. This has also enabled the development of a fast methods for evaluating (2) for a single wall, based on either the (flexible periodicity) Fast Multipole Method [26, 27], or Fast Fourier Transform [28]. For triply-periodic (TP) domains, the Positively Split Ewald (PSE) method [24] for evaluating (2) (and also generating Brownian velocities [24]) for the RPY kernel provides the basis for Fast Stokesian Dynamics [14]. However, it remains a challenge to construct a similarly-efficient method for confined suspensions since PSE uses Fourier representations in a key way in all components of the method (Stokes solver, generating Brownian increments, and Ewald splitting).

In principle, a greater flexibility with respect to boundary conditions can be achieved by replacing analytical Green's functions with a grid-based Stokes solver [29]. This requires replacing the singular surface delta function form of $\delta_a(\mathbf{r})$ with a smooth function that can be resolved on a grid. In FCM, a Gaussian envelope function δ_a is used, which allows for analytical calculation of \mathcal{R} in an unbounded domain [5, 6]; in numerical methods the Gaussian is truncated. By contrast, in the Immersed Boundary Method (IBM) δ_a is a discrete grid function specifically constructed to maximize grid invariance [11, 16, 30], and the double convolution in (1) is discrete. This makes all IBM results grid- and solver-dependent, without a direct continuum limit.

In this paper we develop a method that combines favorable features of FCM and IBM. Namely, we maintain the continuum representation (1) from FCM, however, we do not use a Gaussian envelope but rather use the “exponential of a semi-circle” kernel proposed by Barnett for the purpose of non-uniform FFT [10]. This not only allows greater flexibility in tuning the hydrodynamic radius of the particles [31], but also allows us to use many fewer grid cells per particle than for a Gaussian kernel, comparable to the IBM, while still solving the continuum equations to several digits of accuracy. Specifically, for about three digits of accuracy we require 4 grid cells per dimension if only translational velocity is required, and five or six if rotational velocities are also required. The grid independence of the results makes them transferable, and allows us to separate the Stokes solver from the FCM method itself. We employ an image construction following Yeo and Maxey [7] (also used in the IBM [16, 32]) to generalize (1) to the relevant-in-practice case when some of the blob kernels overlap the boundaries; this is considerably harder to do for the RPY kernel, and has required *ad hoc* fixes in past work by some of us [33].

For TP domains one can easily solve the Stokes equations spectrally in Fourier space. Here we use some of the ideas applied to the Poisson equation in [12] to develop a Stokes solver for doubly-periodic (DP) geometries that are unbounded or confined by one or two boundaries in the aperiodic direction. Here we focus on *bottom wall* (BW) DP geometries, with a single no-slip wall at $z = 0$, and *slit channel* (SC) DP geometry, confined by no-slip walls at $z = 0$ and $z = H$, but the Stokes solver can handle more flexible boundary conditions in the aperiodic direction. Our novel fluid solver makes it possible to handle geometries that are partially unbounded in one direction, unlike in existing IBM or FCM implementations based on more traditional grid solvers like finite differences or finite elements [34]. Our fluid solver has the additional advantage that its implementation requires only calls to the three-dimensional (3D) FFT with an oversampling factor of 2 in the aperiodic direction, combined with trivially parallelizable one-dimensional boundary value solvers in the z direction. We use this to implement the method on Graphical Processing

Unit, achieving linear scaling up to as many as one million particles, with constants much better than existing fast methods [27] for the types of problems we study here. It is important to note that Srinivasan and Tornberg have developed a sophisticated method based on 3D FFTs for the singular Stokes Green's function for an unbounded bottom wall geometry (using images) [28]. Our approach is different and specialized to doubly-periodic geometries, and is conceptually simpler and affords flexibility in the boundary conditions in the unbounded direction. It is beyond the scope of this work to give a thorough comparison of the different approaches.

In this work we study how to choose the parameters of the ES kernel to achieve a desired accuracy and effective blob hydrodynamic radius with the coarsest possible solver grid. We also perform a number of validation tests examining the self and pair mobility of particles in BW and SC geometries, and show that the method produces results in agreement with existing theoretical or numerical predictions. We also demonstrate that it is possible to generate stochastic (Brownian) particle displacements with covariance proportional to \mathcal{M} using a Lanczos method [35, 36] in a modest number of iterations independent of the number of particles, for both BW and SC geometries. This allows us to replace the core hydrodynamic routines used in the Stokesian dynamics method developed in [21] and the rigid multiblob Brownian Dynamics methods developed in [17] with new linear-scaling implementations that are substantially more efficient for sufficiently large number of particles. These new computational developments enable us to perform larger-scale studies of the dynamics of confined microroller suspensions than previously feasible.

II. MODEL FORMULATION

We develop a method to solve the Stokes equations,

$$\eta \nabla^2 \mathbf{u} - \nabla p = -\mathbf{f}, \quad (4)$$

$$\nabla \cdot \mathbf{u} = 0, \quad (5)$$

in an xy doubly-periodic domain of size $[x \ y] \in [-L_x, L_x] \times [-L_y, L_y]$,¹ with $z \in [0, \infty)$; we refer to this as a *bottom wall* (BW) geometry. We will return later to the case of a *slit channel* (SC) geometry with two walls at $z = 0$ and $z = H$, for which $z \in [0, H]$. Here $\mathbf{u} = [u \ v \ w]$ is the velocity field of the fluid, p the pressure, η the viscosity, and the body force $\mathbf{f} = [f \ g \ h]$ represents particles. To close the problem, we impose tangential slip boundary conditions (BCs) at $z = 0$, i.e.,

$$\mathbf{u}|_{z=0} = \mathbf{u}^{\text{wall}} = [u^{\text{wall}} \ v^{\text{wall}} \ 0], \quad (6)$$

where $\mathbf{u}^{\text{wall}}(x, y)$ is a smooth function giving a prescribed slip velocity ($\mathbf{u}^{\text{wall}} = \mathbf{0}$ for no-slip boundaries) along the wall, and we require boundedness of \mathbf{u} as $z \rightarrow \infty$.

The source term \mathbf{f} is restricted to the domain limits (i.e. $\mathbf{f}(z \notin [0, H]) = 0$) and consists of regularized monopoles and dipoles with envelope functions Δ_M and Δ_D centered around particles or blobs, i.e.,

$$\mathbf{f}(\mathbf{x}) = \sum_{j=1}^N \left[\mathbf{F}^{(j)} \Delta_M(\mathbf{x} - \mathbf{r}^{(j)}) + \frac{1}{2} \nabla \times (\boldsymbol{\tau}^{(j)} \Delta_D(\mathbf{x} - \mathbf{r}^{(j)})) \right], \quad (7)$$

where $\mathbf{x} = [x \ y \ z]$ and $\mathbf{r}^{(j)} = [x^{(j)} \ y^{(j)} \ z^{(j)}]$ is the j th particle's location with $j = 1, \dots, N$, and $\mathbf{F}^{(j)}$ and $\boldsymbol{\tau}^{(j)}$ are the force and torque of the j th particle. Here, Δ_M and Δ_D are compactly-supported, smooth, regularized delta functions called kernels in the immersed boundary method (IBM), or envelopes in the Fast Coupling Method (FCM). In the classical FCM, the envelopes are (truncated) Gaussians,

$$\Delta_{M/D}(\mathbf{x}) = \frac{1}{\sqrt{8\pi^3 g_{M/D}^6}} \exp\left(-\frac{\|\mathbf{x}\|^2}{2g_{M/D}^2}\right), \quad (8)$$

where $g_M = R_h/\sqrt{\pi}$ and $g_D = R_h/(6\sqrt{\pi})^{\frac{1}{3}}$, with R_h as the effective hydrodynamic radius of a particle/blob.

If a particle is closer to the wall than a distance z_{im} so that its kernel overlaps the wall, we add the negative of the particle's envelope centered at its image point about the wall. This ensures that the force/torque decays to zero as a particle approaches the wall. As a result, if $z^{(j)} < z_{\text{im}}$, we replace the envelopes Δ_M and Δ_D in (7) with

$$\Delta_{M/D}^W(\mathbf{x} - \mathbf{r}^{(j)}) = \Delta_{M/D}(\mathbf{x} - \mathbf{r}^{(j)}) - \Delta_{M/D}(\mathbf{x} - \mathbf{r}_{\text{im}}^{(j)}), \quad (9)$$

¹ For our results, we consider a square domain in xy plane for simplicity, i.e., $L_{x/y} = L$.

where $\mathbf{r}_{\text{im}}^{(j)} = \mathbf{r}^{(j)} - 2\hat{\mathbf{e}}_z(\hat{\mathbf{e}}_z \cdot \mathbf{r}^{(j)})$ is the particle's point of reflection about the bottom wall, and $\hat{\mathbf{e}}_z = [0 \ 0 \ 1]$. In the FCM, Yeo and Maxey [7] put a positive sign in (9) for Δ_D , to ensure that the angular velocity of a particle in simple shear flow is unaffected by the proximity to the wall. We put a negative sign to ensure that all components of the particle mobility go to zero at the wall. This is a modeling choice, and it is important to realize that (9) is not an exact image construction for a no-slip wall [28]. For a free-slip boundary such as a gas-liquid interface, it is straightforward to make an exact image construction; see, for example, Appendix A in [37].

Our goal is to compute the motion of each of the particles for dynamical simulations. Suppose we've solved the Stokes equations for the fluid velocity \mathbf{u} , then the linear and angular velocities of the particles, denoted as $\mathbf{U}^{(j)}$ and $\boldsymbol{\Omega}^{(j)}$, can be obtained through the following volume integrals over the envelopes,

$$\mathbf{U}^{(j)} = \int_{\mathbf{x}} \mathbf{u}(\mathbf{x}) \Delta_M(\mathbf{x} - \mathbf{r}^{(j)}) d\mathbf{x}, \quad (10)$$

$$\boldsymbol{\Omega}^{(j)} = \frac{1}{2} \int_{\mathbf{x}} (\nabla \times \mathbf{u}(\mathbf{x})) \Delta_D(\mathbf{x} - \mathbf{r}^{(j)}) d\mathbf{x}, \quad (11)$$

with the understanding that $\Delta_{M/D}$ get replaced by $\Delta_{M/D}^W$ for particles close to a wall.

In our own variant of FCM, we will not use a Gaussian kernel; rather, we will employ a compactly-supported Exponential of a Semicircle (ES) kernel [10] optimized for numerical efficiency in spectral methods, as we discuss in detail in Sec. III E. Other kernels can be used as well, as long as their Fourier transform decays exponentially fast in the wavenumber.

III. STOKES PROBLEM

We develop a doubly-periodic+correction Stokes solver based on the observation that, the original problem (4)–(5) can be separated into two subproblems, namely the doubly-periodic “DP” problem and the “correction” problem. For the DP subproblem, we keep the source terms \mathbf{f} but there is no wall present (i.e., open BCs in z). The correction subproblem, has the walls but has no forcing, so it can be solved analytically using a plane-wave expansion. The total solution is then the sum of the solutions to the two subproblems.

Below, we detail our solution method for the bottom wall (BW) geometry with a no-slip wall. Appendix A summarizes the method for the slit channel (SC) geometry with somewhat more general partial slip BCs. The Stokes solver can also handle open boundaries in the z direction, if the total force on the domain is zero. In order to uniquely define the self mobility of a particle, one must therefore add a negative tail to the kernel to account for the *backflow* around the particle, similar to how in TP domains the $[k_x \ k_y \ k_z] = \mathbf{0}$ component of the solution is set to zero. We defer discussion of backflow in unbounded DP geometries to future work.

A. Doubly-periodic Stokes solver

For the “DP” subproblem, we solve a doubly-periodic Stokes problem for \mathbf{u}_{DP} and p_{DP} :

$$\eta \nabla^2 \mathbf{u}_{\text{DP}} - \nabla p_{\text{DP}} = -\mathbf{f}, \quad (12)$$

$$\nabla \cdot \mathbf{u}_{\text{DP}} = 0. \quad (13)$$

Here the source term \mathbf{f} is the same as (4), and the doubly-periodic domain is $[x \ y \ z] \in [-L_x, L_x] \times [-L_y, L_y] \times (-\infty, +\infty)$ with *free-space* BCs in z , i.e., p_{DP} and \mathbf{u}_{DP} are bounded as $z \rightarrow \pm\infty$ and there is no wall present. Note that in our spectral DP solver, we will solve \mathbf{u}_{DP} in a bounded domain $[x \ y \ z] \in [-L_x, L_x] \times [-L_y, L_y] \times [0, H]$ for either bottom wall or slit channel geometry. For a slit channel, 9 ensures that $\mathbf{f} = \mathbf{0}$ is smooth on and vanishes outside of $z \in [0, H]$, and for bottom wall case, we will assume that it is possible to find a maximum height H , so that \mathbf{f} smoothly goes to zero for $z > H$. As we now show, the open boundary condition can be reduced to $z \in [0, H]$ through the Dirichlet-to-Neumann map, as proposed for the Poisson equation by Maxian et al. [12].

1. Solution for p_{DP}

First take the divergence of (12) and use (13) to obtain

$$\nabla^2 p_{\text{DP}} = \nabla \cdot \mathbf{f}. \quad (14)$$

Fourier transforming in the xy domain yields

$$(\partial_z^2 - k^2) \hat{p}_{\text{DP}}(\mathbf{k}, z) = [\mathbf{i}\mathbf{k} \quad \partial_z] \cdot \hat{\mathbf{f}}(\mathbf{k}, z). \quad (15)$$

Here $[k_x \ k_y] = [n_x \ n_y] \pi/L_{x/y}$ with $n_{x/y} \in \mathbb{Z}$, and $k = \|\mathbf{k}\|$. For $z \notin [0, H]$, $\mathbf{f} = \mathbf{0}$ and the general solution to (15) is

$$\hat{p}_{\text{DP}}(\mathbf{k}, z \geq H) = C_1 e^{-kz}, \quad \hat{p}_{\text{DP}}(\mathbf{k}, z \leq 0) = C_2 e^{kz}, \quad (16)$$

where we used the boundedness of \hat{p}_{DP} as $z \rightarrow \pm\infty$. The solutions (16) imply simple Dirichlet-to-Neumann maps for \hat{p}_{DP} at $z = 0^-$ and $z = H^+$. Since \hat{p}_{DP} is continuously differentiable across the computational boundaries at $z = 0$ and $z = H$, the same maps apply at $z = H^-$ and $z = 0^+$ as well, giving

$$(\partial_z + k) \hat{p}_{\text{DP}}(\mathbf{k}, z = H) = 0, \quad (\partial_z - k) \hat{p}_{\text{DP}}(\mathbf{k}, z = 0) = 0. \quad (17)$$

Therefore, we can solve the boundary value problem (BVP) (15) on $z \in [0, H]$ subject to the boundary conditions given by (17). This approach was proposed by some of us for the Poisson equation in [12].

2. Solution for \mathbf{u}_{DP}

To find the velocity, we take an xy Fourier transform of (12):

$$-\eta (\partial_z^2 - k^2) \hat{u}_{\text{DP}}(\mathbf{k}, z) + [\mathbf{i}\mathbf{k} \quad \partial_z] \hat{p}_{\text{DP}}(\mathbf{k}, z) = \hat{\mathbf{f}}(\mathbf{k}, z). \quad (18)$$

Again, $\mathbf{f} = \mathbf{0}$ outside domain $z \in [0, H]$, giving

$$\partial_z^2 \hat{u}_{\text{DP}} - k^2 \hat{u}_{\text{DP}} = \frac{\mathbf{i}k_x}{\eta} \hat{p}_{\text{DP}}, \quad (19)$$

$$\partial_z^2 \hat{w}_{\text{DP}} - k^2 \hat{w}_{\text{DP}} = \frac{1}{\eta} \partial_z \hat{p}_{\text{DP}}. \quad (20)$$

Using the solution for \hat{p}_{DP} in (16), and enforcing boundedness of \hat{u}_{DP} as $z \rightarrow \pm\infty$, we find the general solution for $\mathbf{k} \neq \mathbf{0}$,

$$\hat{u}_{\text{DP}}(\mathbf{k}, z \geq H) = A_x e^{-kz} - \frac{\mathbf{i}k_x C_1}{2k\eta} z e^{-kz}, \quad (21a)$$

$$\hat{u}_{\text{DP}}(\mathbf{k}, z \leq 0) = B_x e^{kz} + \frac{\mathbf{i}k_x C_2}{2k\eta} z e^{kz}. \quad (21b)$$

Due to xy symmetry of the problem, solutions to \hat{v}_{DP} are analogous and obtained by replacing x with y in (21).

From (21), we get the following Dirichlet-to-Neumann maps at the boundaries:

$$(\partial_z + k) \begin{bmatrix} \hat{u}_{\text{DP}}(\mathbf{k}, H) \\ \hat{v}_{\text{DP}}(\mathbf{k}, H) \end{bmatrix} = -\frac{\mathbf{i}\mathbf{k}}{2k\eta} \hat{p}_{\text{DP}}(\mathbf{k}, H), \quad (\partial_z - k) \begin{bmatrix} \hat{u}_{\text{DP}}(\mathbf{k}, 0) \\ \hat{v}_{\text{DP}}(\mathbf{k}, 0) \end{bmatrix} = \frac{\mathbf{i}\mathbf{k}}{2k\eta} \hat{p}_{\text{DP}}(\mathbf{k}, 0). \quad (22)$$

Similarly, the general solution for \hat{w}_{DP} is

$$\hat{w}_{\text{DP}}(\mathbf{k}, z \geq H) = A_z e^{-kz} + \frac{C_1}{2\eta} z e^{-kz}, \quad (23a)$$

$$\hat{w}_{\text{DP}}(\mathbf{k}, z \leq 0) = B_z e^{kz} + \frac{C_2}{2\eta} z e^{kz}. \quad (23b)$$

which implies the following boundary conditions:

$$(\partial_z + k) \hat{w}_{\text{DP}}(\mathbf{k}, H) = \frac{1}{2\eta} \hat{p}_{\text{DP}}(\mathbf{k}, H), \quad (\partial_z - k) \hat{w}_{\text{DP}}(\mathbf{k}, 0) = \frac{1}{2\eta} \hat{p}_{\text{DP}}(\mathbf{k}, 0). \quad (24)$$

We can solve the BVP problems (18) on $z \in [0, H]$ with boundary conditions (22) and (24) to find the velocity field using a spectral (Chebyshev) solver, as described in Sec. III D.

B. Correction solve

The correction subproblem solves the following homogeneous Stokes problem for \mathbf{u}_{corr} and p_{corr} ,

$$\eta \nabla^2 \mathbf{u}_{\text{corr}} - \nabla p_{\text{corr}} = 0, \quad (25)$$

$$\nabla \cdot \mathbf{u}_{\text{corr}} = 0, \quad (26)$$

where the doubly-periodic domain is $[x \ y \ z] \in [-L_x, L_x] \times [-L_y, L_y] \times [0, +\infty]$ and with slip on the bottom wall

$$\mathbf{u}_{\text{corr}}|_{z=0} = \mathbf{u}^{\text{wall}} - \mathbf{u}_{\text{DP}}|_{z=0}, \quad (27)$$

where \mathbf{u}_{DP} is the solution to the DP problem. Note that, by linearity, it is clear that the sum of the solution to the two subproblems in the upper-half plane gives the solution to the original problem (4)–(6), i.e.,

$$\mathbf{u} = \mathbf{u}_{\text{DP}} + \mathbf{u}_{\text{corr}}, \quad \text{and} \quad p = p_{\text{DP}} + p_{\text{corr}}. \quad (28)$$

The correction subproblem (25)–(27) can be solved analytically.

1. Solution for p_{corr}

Taking divergence of (25) we obtain a Laplace equation for pressure

$$\Delta p_{\text{corr}} = 0. \quad (29)$$

After a Fourier transform in xy , we get a 1D equation for each Fourier mode \mathbf{k} ,

$$\partial_z^2 \hat{p}_{\text{corr}}(\mathbf{k}, z) - k^2 \hat{p}_{\text{corr}}(\mathbf{k}, z) = 0. \quad (30)$$

Using the boundedness of \hat{p}_{corr} as $z \rightarrow \infty$, the general solution of (30) is

$$\hat{p}_{\text{corr}}(\mathbf{k}, z) = C_0 e^{-kz}. \quad (31)$$

2. Solution for \mathbf{u}_{corr}

Taking the Fourier transform of (25) in xy and using (31) we obtain

$$\eta (k^2 - \partial_z^2) \hat{u}_{\text{corr}}(\mathbf{k}, z) = -ik_x C_0 e^{-kz}, \quad (32)$$

$$\eta (k^2 - \partial_z^2) \hat{w}_{\text{corr}}(\mathbf{k}, z) = k C_0 e^{-kz}, \quad (33)$$

with general solutions for $\mathbf{k} \neq \mathbf{0}$ given by

$$\hat{u}_{\text{corr}}(\mathbf{k}, z) = -\frac{C_0 i k_x}{2\eta k} z e^{-kz} + C_x e^{-kz}, \quad (34)$$

$$\hat{w}_{\text{corr}}(\mathbf{k}, z) = \frac{C_0}{2\eta} z e^{-kz} + C_z e^{-kz}, \quad (35)$$

and analogously for \hat{v}_{corr} . To determine the unknown coefficients, we consider the boundary conditions on the wall. Let $\mathbf{u}_{\text{corr}}|_{z=0} = \mathbf{u}^{\text{wall}} - \mathbf{u}_{\text{DP}}|_{z=0} = [u_0(x, y) \ v_0(x, y) \ w_0(x, y)]$, i.e.,

$$\hat{u}_{\text{corr}}(\mathbf{k}, 0) = \hat{u}_0(\mathbf{k}), \quad \hat{v}_{\text{corr}}(\mathbf{k}, 0) = \hat{v}_0(\mathbf{k}), \quad \hat{w}_{\text{corr}}(\mathbf{k}, 0) = \hat{w}_0(\mathbf{k}). \quad (36)$$

Substituting (34)–(35) into (36) gives three of the unknown coefficients:

$$C_x = \hat{u}_0(\mathbf{k}), \quad C_y = \hat{v}_0(\mathbf{k}), \quad C_z = \hat{w}_0(\mathbf{k}). \quad (37)$$

To find the coefficient C_0 we take an xy Fourier transform of (26):

$$ik_x \hat{u}_{\text{corr}}(\mathbf{k}, z) + ik_y \hat{v}_{\text{corr}}(\mathbf{k}, z) + \partial_z \hat{w}_{\text{corr}}(\mathbf{k}, z) = 0. \quad (38)$$

Evaluating (38) at $z = 0$ and also using the boundary conditions (36), we obtain

$$\partial_z \hat{w}_{\text{corr}}(\mathbf{k}, z = 0) = -ik_x \hat{u}_0(\mathbf{k}) - ik_y \hat{v}_0(\mathbf{k}), \quad (39)$$

which coupled with (35) gives

$$C_0 = 2\eta(k\hat{w}_0(\mathbf{k}) - ik_x \hat{u}_0(\mathbf{k}) - ik_y \hat{v}_0(\mathbf{k})). \quad (40)$$

Substituting the coefficients back to (34)–(35), we obtain an explicit correction solution in xy Fourier space:

$$\hat{p}_{\text{corr}}(\mathbf{k}, z) = 2\eta(k\hat{w}_0(\mathbf{k}) - ik_x \hat{u}_0(\mathbf{k}) - ik_y \hat{v}_0(\mathbf{k}))e^{-kz}, \quad (41)$$

$$\hat{u}_{\text{corr}}(\mathbf{k}, z) = -\frac{k_x}{k}(ik\hat{w}_0(\mathbf{k}) + k_x \hat{u}_0(\mathbf{k}) + k_y \hat{v}_0(\mathbf{k}))ze^{-kz} + \hat{u}_0(\mathbf{k})e^{-kz}, \quad (42)$$

$$\hat{v}_{\text{corr}}(\mathbf{k}, z) = -\frac{k_y}{k}(ik\hat{w}_0(\mathbf{k}) + k_x \hat{u}_0(\mathbf{k}) + k_y \hat{v}_0(\mathbf{k}))ze^{-kz} + \hat{v}_0(\mathbf{k})e^{-kz}, \quad (43)$$

$$\hat{w}_{\text{corr}}(\mathbf{k}, z) = (k\hat{w}_0(\mathbf{k}) - ik_x \hat{u}_0(\mathbf{k}) - ik_y \hat{v}_0(\mathbf{k}))ze^{-kz} + \hat{w}_0(\mathbf{k})e^{-kz}. \quad (44)$$

C. Zero mode ($\mathbf{k} = 0$)

Secs. III A and III B provide the DP and correction solutions for $\mathbf{k} \neq \mathbf{0}$. We treat the $\mathbf{k} = \mathbf{0}$ mode here for the overall solution without separating into subproblems.

To find $\hat{w}(\mathbf{0}, z)$, we use the continuity equation (5) in Fourier space for $k_x = k_y = 0$,

$$\partial_z \hat{w}(\mathbf{0}, z) = 0. \quad (45)$$

As a result, $\hat{w}(\mathbf{0}, z)$ is just a constant, and the no-slip boundary conditions at $z = 0$, given in Fourier space by

$$\hat{\mathbf{u}}(\mathbf{k}, 0) = [\hat{u}^{\text{wall}}(\mathbf{k}) \ \hat{v}^{\text{wall}}(\mathbf{k}) \ 0], \quad (46)$$

indicate that

$$\hat{w}(\mathbf{0}, z) = 0. \quad (47)$$

The momentum equation (4) in Fourier space for $\mathbf{k} = \mathbf{0}$ can be expressed as

$$-\eta \partial_z^2 \hat{\mathbf{u}}(\mathbf{0}, z) + [\mathbf{0} \ \partial_z] \hat{p}(\mathbf{0}, z) = \hat{\mathbf{f}}(\mathbf{0}, z) = [\hat{f}(\mathbf{0}, z) \ \hat{g}(\mathbf{0}, z) \ \hat{h}(\mathbf{0}, z)]. \quad (48)$$

Using (47), the z component of (48) simplifies to

$$\partial_z \hat{p}(\mathbf{k} = 0, z) = \hat{h}(\mathbf{k} = 0, z), \quad (49)$$

which yields the zero mode solution for the pressure,

$$\hat{p}(\mathbf{0}, z) = \int_0^z \hat{h}(\mathbf{0}, z') dz', \quad (50)$$

where we set $\hat{p}(\mathbf{0}, 0) = 0$ as a convention.

To find the $\mathbf{k} = \mathbf{0}$ mode solution for \hat{u} (or \hat{v} due to symmetry in xy), note that the x component of (48) is

$$\partial_z^2 \hat{u}(\mathbf{0}, z) = -\frac{\hat{f}(\mathbf{0}, z)}{\eta}. \quad (51)$$

We have a no-slip BC at $z = 0$ given by (46). To find a boundary condition at $z = H$, note that for $z > H$, $\partial_{zz} \hat{u}(\mathbf{0}, z) = 0$, which along with the boundedness of velocity as $z \rightarrow \infty$, indicate that $\hat{u}(\mathbf{0}, z \geq H)$ is some constant. Since $\partial_z \hat{u}(\mathbf{0}, z)$ is continuous across $z = H$ and it is a constant for $z > H$, we conclude that $\partial_z \hat{u}(\mathbf{0}, H) = 0$. As a result, the $\mathbf{k} = \mathbf{0}$ mode of \hat{u} can be computed by solving the BVP (51) with the following boundary conditions:

$$\hat{u}(\mathbf{0}, 0) = \hat{u}^{\text{wall}}(\mathbf{0}), \quad \partial_z \hat{u}(\mathbf{0}, H) = 0, \quad (52)$$

and analogously for \hat{v} .

D. Stokes solver

Our spectral doubly-periodic Stokes solver is based on the method proposed for the Poisson equation in [12], where more details are provided. We use the Fast Fourier Transform (FFT) in the doubly-periodic xy plane and Chebyshev polynomials in the z direction to achieve spectral accuracy. The grid is uniform in the xy plane, with spacing $h_{x/y} = 2L_{x/y}/N_{x/y}$ where $N_{x/y}$ is the total number of points in each direction, and nonuniform in the z direction, with grid points placed on a type-2 Chebyshev grid including the endpoints. The number of Chebyshev grid points, N_z , is chosen such that the coarsest spacing in the z direction (occurring at the midplane) is comparable to $h_{x/y}$ (see Eq. (108) in [12]).

In principle, we could take a 2D FFT of (12) and (14) to find the discrete form of (18) and (15), respectively, and solve the resulting BVPs in the z direction in Chebyshev space. Instead, following Maxian et al. [12], we take advantage of the Chebyshev compatibility with the Fourier transform² and solve the problem in 3D Fourier-Chebyshev space [39]. This allows us to use 3D FFTs in the implementation, which gives greater flexibility for optimizing parallel performance. We have implemented the method in CUDA for Graphical Processing Units (GPUs) in the UAMMD library [40], using the NVIDIA cuFFT library.

The following steps summarize our solution algorithm for the Stokes equation:

- (1) Spread the right hand side (RHS) \mathbf{f} of the momentum equation (12) on the grid using the ES kernel (cf. Sec. III E). Since the ES kernel is compactly supported, each particle only spreads to $\sim w^3$ grid points. In the z direction this is only true if near the midplane; more than w points will be required near the boundaries where the Chebyshev grid is finer. When the kernel extends outside of the domain over a physical boundary,³ we fold the contribution outside of the domain back into the domain using a negative mirror image (see (9)). We will return to spreading torques shortly.
- (2) Take a 3D FFT of \mathbf{f} to compute the Chebyshev coefficients of $\hat{\mathbf{f}}(\mathbf{k}, z)$. Then, use Chebyshev differentiation to compute the Chebyshev coefficients of $\partial_z \hat{\mathbf{f}}(\mathbf{k}, z)$ [39].
- (3) For each $\mathbf{k} \neq \mathbf{0}$, solve the BVP (15) with boundary conditions (17) for the Chebyshev coefficients of $\hat{p}_{\text{DP}}(\mathbf{k}, z)$. Then, evaluate $\hat{p}(\mathbf{k}, z = 0/H)$ by direct summation to assemble boundary conditions (22) and (24), and solve the BVP (18) for the Chebyshev coefficients of $\hat{\mathbf{u}}_{\text{DP}}(\mathbf{k}, z)$. See Appendix A in [12] for details of the BVP solver, which is based on [38].
- (4) Evaluate, by direct summation, $\hat{\mathbf{u}}_{\text{DP}}(\mathbf{k}, z = 0)$ for the BW geometry and also $\hat{\mathbf{u}}_{\text{DP}}(\mathbf{k}, z = H)$ for the SC geometry,⁴ and compute the RHSs of (36) and (A2), respectively. Evaluate the correction solutions, $\hat{p}_{\text{corr}}(\mathbf{k}, z)$ and $\hat{\mathbf{u}}_{\text{corr}}(\mathbf{k}, z)$ on the Chebyshev grid, using the analytical expressions (41)–(44) for BW and (A4)–(A6) for SC geometries.
- (5) Evaluate the $\mathbf{k} = \mathbf{0}$ mode solution for $\hat{p}(\mathbf{0}, z)$ using (50) and Chebyshev integration, and solve the BVP given by (51) and (52) for the BW and (A12) for the SC geometry to find $\hat{u}(\mathbf{0}, z)$, and analogously, $\hat{v}(\mathbf{0}, z)$. Set $\hat{w}(\mathbf{0}, z) = 0$.
- (6) For all \mathbf{k} , take a 1D FFT in the z direction to compute the Chebyshev coefficients of the correction and zero-mode solutions and add them to \hat{p}_{DP} and $\hat{\mathbf{u}}_{\text{DP}}$.
- (7) Back transform to real space using a 3D iFFT to get $p(\mathbf{x})$ and $\mathbf{u}(\mathbf{x})$.
- (8) Interpolate $\mathbf{u}(\mathbf{x})$ at the particle positions via (10) and trapezoidal+Chebyshev quadrature to find the linear velocity of the particles. For each particle, this requires the same grid values (but with additional z -dependent quadrature weights) as in the spreading in step #1.

When torques are also applied, they can be spread in two ways. The first way, which is more straightforward to implement but also more computationally expensive, is to compute the derivatives needed for the curl operator in Fourier-Chebyshev space; this requires an additional forward 3D FFT. Analogously, in the interpolation step, the curl of the velocity is first computed in Fourier-Chebyshev space, and then transferred back to real space with an

² Chebyshev coefficients of a function can be obtained by evaluating its values at the Chebyshev points and taking a Fast Cosine Fourier Transform [38]. Our implementation uses a 3D FFT with $2N_z - 2$ points along the z direction.

³ Kernels must never extend outside open boundaries, which can always be placed at an appropriate z location to ensure this.

⁴ For partial slip walls, also compute $\partial_z \hat{\mathbf{u}}_{\text{DP}}(\mathbf{k}, z = 0/H)$ by Chebyshev differentiation and direct summation.

additional 3D iFFT. These additional FFTs can be avoided by instead using the derivative of the ES kernel to spread and interpolate velocity.⁵ We have employed both of these approaches to spread torques and interpolate velocity in a CPU-based implementation and confirm that both preserve the desired accuracy. Due to the higher implementation complexity of the second approach,⁶ in the GPU code we have presently only implemented the first way.

It is important to emphasize that all steps in the method scale linearly, or log-linearly, in either the number of particles or the number of grid points. The BVP solutions along the z direction require solving pentadiagonal linear systems (see Appendix A in [12]), which makes that step need only a linear amount of memory and computational effort in N_z . Combined with the independence of the BVP solves for each \mathbf{k} , this makes the algorithm particularly well-suited for efficient execution on GPUs.

E. Exponential of a semicircle kernel (ES)

In order to reduce the costs associated with representing particles on the grid, we replace the Gaussian kernel traditionally used in the FCM formulation with the exponential of a semicircle (ES) kernel [10]. Specifically, as in the IBM, we take $\Delta_{M/D}$ to be tensor products of a scalar kernel ϕ :

$$\Delta_{M/D}(\mathbf{x}; \alpha_{M/D}, \beta_{M/D}) = \prod_{i=1}^3 \phi(x_i; \alpha_{M/D}, \beta_{M/D}), \quad (53)$$

where

$$\phi(z; \alpha, \beta) = \left(\int_{-\alpha}^{\alpha} e^{\beta(\sqrt{1-(\frac{z}{\alpha})^2}-1)} dz \right)^{-1} \begin{cases} e^{\beta(\sqrt{1-(\frac{z}{\alpha})^2}-1)}, & |z| \leq \alpha \\ 0, & \text{otherwise.} \end{cases} \quad (54)$$

Here, (α, β) are fixed parameters uniquely tied to the kernel, which is compactly supported on $[-\alpha, \alpha]$. If the kernel we use for spreading and interpolation has a simple Fourier transform, we can determine the effective hydrodynamic radius R_h of a particle represented by such a kernel analytically. For example, in the seminal works on FCM applied to Stokes flow [5, 6], the authors show that for Gaussian monopole and dipole envelopes given by (7) with standard deviations g_M and g_D , the length scale of the kernels is related to the particle radius through $g_M = R_h/\sqrt{\pi}$ and $g_D = R_h/(6\sqrt{\pi})^{1/3}$. However, the ES kernel does not have a known analytical Fourier transform, so we will numerically determine the relationship between R_h and (α, β) .

Let us denote with w the number of grid cells in the support of the kernel in each dimension. For a regular grid of spacing h , $\alpha \leq \frac{1}{2}hw$ for the ES kernel, but we typically take $\alpha = \frac{1}{2}hw$. Kernels like the Peskin kernels used in IBM [30] have no free parameters to change R_h once w is chosen. In contrast, the ES kernel affords increased flexibility with the additional parameter β . So, particles of different radii can be represented with the same support α , but different β values. Moreover, the ES kernel has numerically compact support (to some tolerance) in real and Fourier space, and is, therefore, well suited for spectral discretizations of the Stokes problem. That is, the discrete RHS of the Stokes problem (4) will decay rapidly in Fourier space.

A sphere of radius R_h will translate and rotate with linear and angular velocities \mathbf{U} and $\boldsymbol{\Omega}$ in an *unbounded* space under the action of a force $\mathbf{F} = 6\pi\eta R_h \mathbf{U}$ and torque $\boldsymbol{\tau} = 8\pi\eta R_h^3 \boldsymbol{\Omega}$. For a TP domain with a cubic box of size L^3 , periodic corrections to Stokes' law can be expressed as an asymptotic expansion in R_h/L ,

$$\mathbf{F} \approx \frac{6\pi\eta R_h \mathbf{U}}{1 - K_M \frac{R_h}{L}}, \quad \boldsymbol{\tau} \approx \frac{8\pi\eta R_h^3 \boldsymbol{\Omega}}{1 - K_D \left(\frac{R_h}{L}\right)^3}, \quad (55)$$

to leading order, where, K_M and K_D are constants independent of R_h and L . The same form applies to doubly-periodic domains as well with L , but with different constants; in this section we use a TP system so that the grid spacing h is uniform.

For the ES kernel, by scaling invariance under changing the unit of length, there exists a function $c(\beta)$ such that

$$R_h(\alpha, \beta) = c(\beta) (2\alpha). \quad (56)$$

⁵ Since the derivative of the ES kernel is unbounded near the boundaries of its support, we have implemented this by truncating the derivative to zero for arguments with magnitude larger than the point where the derivative has minimal magnitude.

⁶ In particular, it requires using a different kernel along different dimensions. Additionally, to ensure all components of the particle mobility go to zero at a wall, we must use a positive sign for the mirror image for the z partial derivative of the ES kernel.

To obtain $c(\beta)$ empirically, and determine an “optimal” β , we take a single particle in a TP domain and apply a unit force or torque on it, and measure its linear and angular velocities. If we keep the position of the particle (relative to the grid) and α fixed, we can use extrapolation to $L \rightarrow \infty$ based on (55) to obtain R_h . Due to numerical errors, R_h varies slightly based on the exact position of the particle relative to the grid, resulting in numerical loss of translational invariance. In Fig. 1 we show $c(\beta)$ estimated from the mean $\langle R_h \rangle$, along with a polynomial fit. We emphasize that $c(\beta)$ is an intrinsic property of the ES kernel, and is independent of the Stokes solver used, as long as the solver is sufficiently accurate. This is assured to about three digits by our use of a spectral solver for any $w \geq 4$; smaller w have too few points per particle to resolve the envelope. The loss of translational invariance is purely numerical and gets worse for smaller w .

In Fig. 2, we evaluate percent errors in the extrapolated radii at each w and for each β in terms of a 95% confidence interval. That is, we report

$$\%-\text{error} = \frac{4\sigma(w)}{\langle R_h(w) \rangle} \times 100\%, \quad (57)$$

in which $\sigma(w)$ is the standard deviation from the mean radius $\langle R_h(w) \rangle$. We see that for the monopole, $w = 12$ and $\beta/w \approx 1.9$ gives the smallest %-error, while for the dipole, $w = 12$ and $\beta/w \approx 1.7$ are the optimal settings. From the extrapolation for these highly resolved settings, we find $K_M = 2.83$ and $K_D = 4.19$.⁷

Note, in practice and for the sake of efficiency, we use $w = 4, 5, 6$, for which $\beta/w \approx 1.75$ and $\beta/w \approx 1.6$ are optimal settings for the monopole and dipole kernels, respectively. This is to be compared to the optimal value $\beta/w \approx 2.7$ suggested by Barnett et al. [10] for the non-uniform FFT algorithm. The precise values of β and w for each particle species need to be selected by balancing several considerations. First, decreasing $R_h/h = c(\beta)w$ means fewer grid cells in the support of the particle kernel, and therefore, higher efficiency. However, translational invariance ought to be preserved to some target tolerance, requiring keeping β/w in a narrow range around the minima of error seen in Fig. 2. Lastly, L/h must be an integer, preferably an FFT-friendly integer. In this work, we aim for 2–3 digits of accuracy. A final challenge is that the hydrodynamic radius needs to be matched between the monopole and dipole terms. If we use $w = 4$ for the monopole, which is the smallest possible to ensure sufficient grid invariance, we find that we require $w \geq 5$ for the dipole to match R_h and get acceptable accuracy. Table I summarizes values we suggest

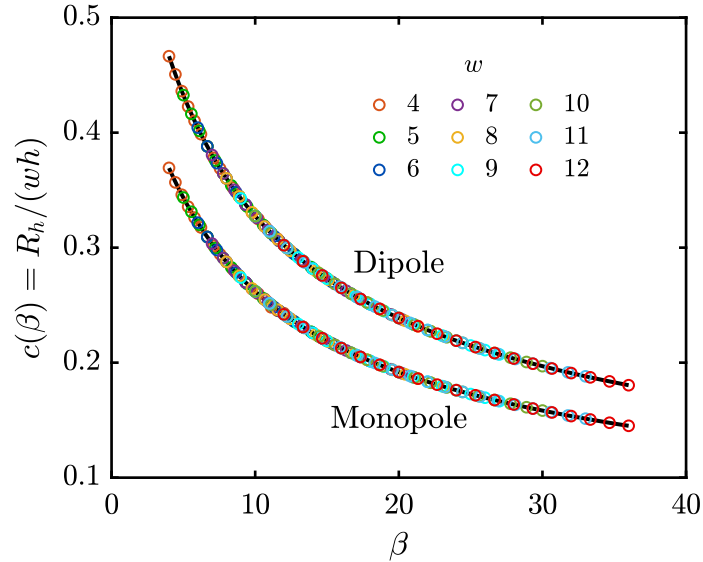


FIG. 1. Dimensionless hydrodynamic radius function $c(\beta)$ for the ES kernel for translation and rotation. We extrapolate to $L \rightarrow \infty$ the computed radii for 30 particle positions distributed uniformly in one grid cell, and for several values of w and β . Specifically, we take $h = 1$, $L \in \{60, 95, 130, 165, 200\}$, $w \in \{4, 5, 6, 7, 8, 9, 10, 11, 12\}$, and β/w values linearly spaced in $[1, 3]$. All of the data collapse on a master curve (depicted in solid black) that can be fit by a polynomial, up to a small error due to loss of translational invariance.

⁷ The value of K_m compares well to the first term in the higher order periodic correction of Hasimoto [41]. The value of K_D is also very close to $4\pi/3$ as predicted in [42] but with an opposite sign, which we believe to be a misprint in [42].

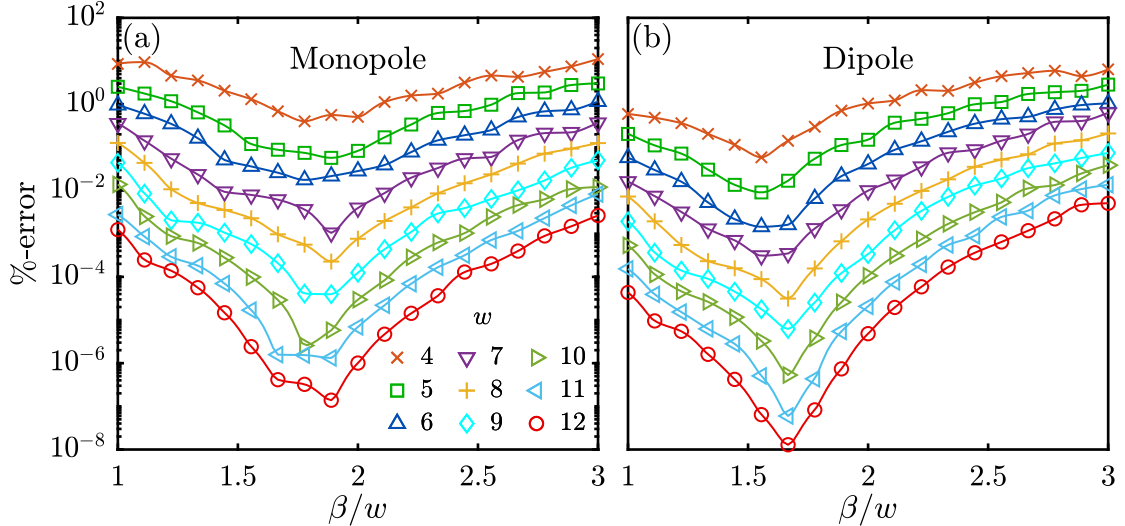


FIG. 2. Percent error (variability) in the effective hydrodynamic radius of a particle represented by the ES kernel as the particle moves relative to an underlying triply-periodic (TP) uniform grid of spacing h . For a given width w , there is an optimal β/w which yields the smallest spread in the calculated effective radius (caused by the loss of translational invariance).

for $w = 5$ and $w = 6$ (it is best to keep w the same for the monopole and dipole kernels). When only translational motion is required (e.g., with the rigid multiblob method [16]), $w = 4$ can be used; Table II summarizes the suggested values. Our public domain software release contains a script that suggests “good” values for w and β given L and R_h as inputs. When there are more than one particle species, the selection becomes more involved but still possible [31].

TABLE I. Optimal combinations of $w_M, w_D, \beta_M, \beta_D$ along with minimal errors and effective radii when both force and torque are applied ($M \& D$).

$w_M (= w_D)$	5	6
R_h/h	1.560	1.731
β_M/w_M	1.305	1.327
β_D/w_D	2.232	2.216
% error _M	0.897	0.151
% error _D	0.810	0.212

TABLE II. Optimal combinations of w_M, β_M along with minimal errors and effective radii when only forces are applied (M).

w_M	4	5	6
R_h/h	1.205	1.344	1.554
β_M/w_M	1.785	1.886	1.714
% error _M	0.370	0.055	0.021

IV. SELF AND PAIR MOBILITIES

In this section, we validate our solver against theoretical predictions on basic mobility problems in the bottom wall (BW) and slit channel (SC) geometries with $N = 1$ or $N = 2$ particles. Specifically, for several particle configurations, we determine the mobility matrix $\mathcal{M} \in \mathbb{R}^{6N \times 6N}$, relating velocities to forces,

$$\begin{bmatrix} \mathbf{U} \\ \boldsymbol{\Omega} \end{bmatrix} = \begin{bmatrix} \mathcal{M}^{tt} & \mathcal{M}^{tr} \\ \mathcal{M}^{rt} & \mathcal{M}^{rr} \end{bmatrix} \begin{bmatrix} \mathbf{F} \\ \boldsymbol{\tau} \end{bmatrix}, \quad (58)$$

where $\mathcal{M}^{(..)} \in \mathbb{R}^{3N \times 3N}$ with superscripts t and r denoting the translational and rotational mobility components, respectively, and $\mathbf{F}, \boldsymbol{\tau} \in \mathbb{R}^{3N}$ and $\mathbf{U}, \boldsymbol{\Omega} \in \mathbb{R}^{3N}$ are the vectors of force and torque on the particles and the resulting translation and rotational velocities. We will refer to certain elements of \mathcal{M} using the notation μ_{ab}^{cd} . This corresponds to prescribing a force or torque ($d = t$ or r) in the b direction ($b = x, y$ or z) on one particle, and measuring the linear or rotational velocity ($c = t$ or r) in the a direction on the second particle (or the same particle, in the case of self mobility). For example, μ_{yx}^{tr} corresponds to the linear velocity in the y direction of the second particle due to a torque about the x axis on the first particle, i.e., $U_y^{(2)} = \mu_{yx}^{tr} \tau_x^{(1)}$.

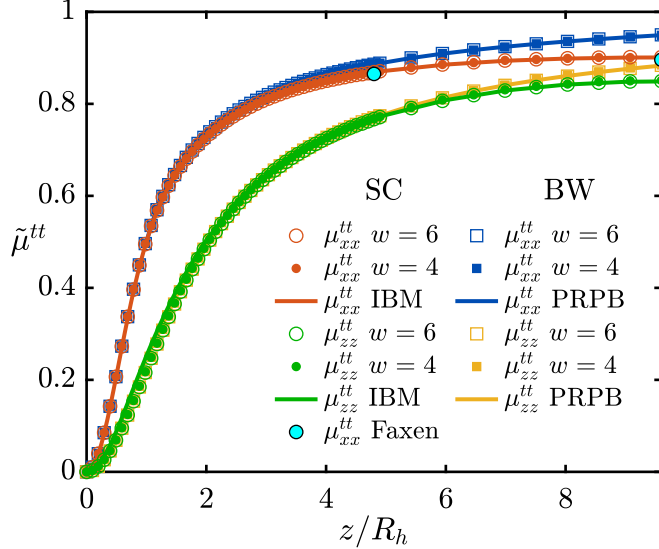


FIG. 3. Normalized translation-translation self mobility, $\tilde{\mu}^{tt} = (6\pi\eta R_h) \mu^{tt}$, above the lower wall ($z \in [0, \frac{1}{2}H]$) in the bottom wall (BW) and slit channel (SC) geometries for $w = 6$ (empty markers) and $w = 4$ (filled markers). The reference data (shown with solid curves) for the BW and SC geometries are from a periodized Rotne-Prager-Blake (PRPB) tensor and numerical results from the immersed boundary method (IBM) [16], respectively. Faxen's results for μ_{xx}^{tt} at $z = \frac{1}{4}H$ and $z = \frac{1}{2}H$ in the SC geometry are shown in cyan circles.

In all tests, we use a box with dimensions $L_{x/y} = L = 76.8R_h$, $H = 19.2R_h$ to allow direct comparison with prior IBM results [16]. The components of \mathcal{M}^{tt} , $\mathcal{M}^{tr/rt}$, and \mathcal{M}^{rr} are normalized by $1/(6\pi\eta R_h)$, $1/(6\pi\eta R_h^2)$, and $1/(8\pi\eta R_h^3)$, respectively. For problems involving rotation, we use the $w_M = w_D = 6$ optimal ES monopole and dipole kernels (cf. Table I). If the problem only involves translation, we can use the optimal $w_M = 4$ monopole kernel (cf. Table II).

A. Self mobility

In this section, we examine the behavior of the linear and rotational velocity of a particle given some prescribed forces or torques, for several particle positions relative to the wall(s), in both the BW and SC geometries.

First, we consider translation-translation self mobility. In the bottom wall (BW) geometry, we compare our numerical results to the periodized Rotne-Prager-Blake (PRPB) tensor. The RPB formulas [22] are for a half-space with no-slip conditions on the bottom wall, valid only for $z \geq R_h$. We periodize them by directly summing over 400 images in the x and y directions to account for the periodic boundary conditions in our doubly-periodic simulations (400^2 images in total). We also compare to Faxen's power series expansions for the parallel self translational mobility of a sphere at half and quarter channel locations (see Eq. (24) in [32]). In Fig. 3, we plot the parallel $\mu_{\parallel}^{tt} = \mu_{xx}^{tt} = \mu_{yy}^{tt}$ and perpendicular $\mu_{\perp}^{tt} = \mu_{zz}^{tt}$ self mobilities of a blob. All of our numerical results agree with the corresponding references values for both $w = 4$ and $w = 6$ for $z \gtrsim 2R_h$. By the image construction (9), the particle mobility goes to zero smoothly as $z \rightarrow 0$ for both the FCM and IBM, but in a kernel/solver dependent manner. Nevertheless, only small differences in μ_{zz}^{tt} near the wall are noticeable in the figure between the RPB, IBM, and FCM mobilities.

In Fig. 4 we show the parallel $\mu_{\parallel}^{rr} = \mu_{xx}^{rr} = \mu_{yy}^{rr}$ and perpendicular $\mu_{\perp}^{rr} = \mu_{zz}^{rr}$ mobility components of \mathcal{M}^{rr} . Again, our numerical results are in excellent agreement with the reference evaluations for $z \gtrsim 2R_h$. Since the wall corrections to the rotational components of the free space RPY tensor in the RPB tensor decay fast like $(R_h/z)^3$, μ_{xx}^{rr} and μ_{zz}^{rr} in BW geometry are nearly indistinguishable from the same components in SC geometry. As the blob approaches the wall, we see a noticeable difference between RPB and FCM for μ_{xx}^{rr} . Lacking a reference result from other methods, in the SC geometry, we compare to a numerical reference computation on a doubly refined grid (i.e., $h := \frac{1}{2}h$ and $w := 2w$ such that the support α remains constant).

In Fig. 5 we show μ_{yx}^{tr} , a translation-rotation self coupling component of \mathcal{M}^{tr} . Interestingly, the mobility does not decay to zero as $z \rightarrow \infty$, as it would for a half-space domain; we display the non-periodized RPB kernel as dashed red lines in the left panel to highlight the effect of periodic boundary conditions in x, y . Furthermore, our numerical

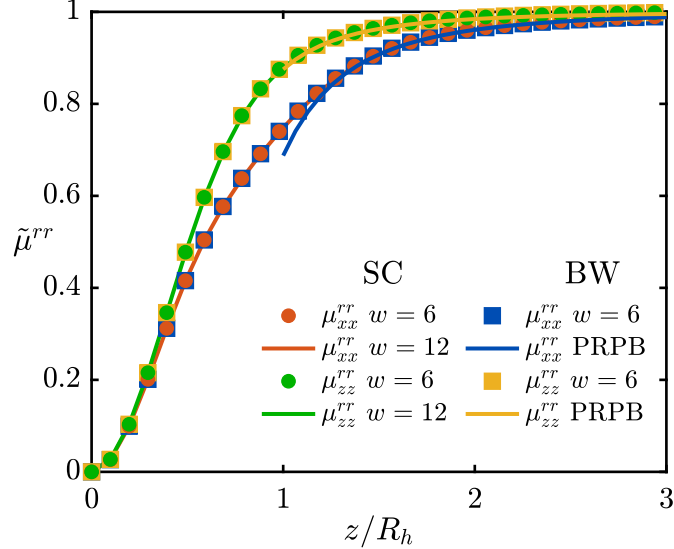


FIG. 4. Normalized rotation-rotation self mobility, $\tilde{\mu}^{rr} = (8\pi\eta R_h^3) \mu^{rr}$, above the lower wall at $z = 0$ in the BW and SC geometries. The reference results, from PRPB for the BW geometry and a twice resolved grid ($w = 12$) for the SC geometry, are solid curves.

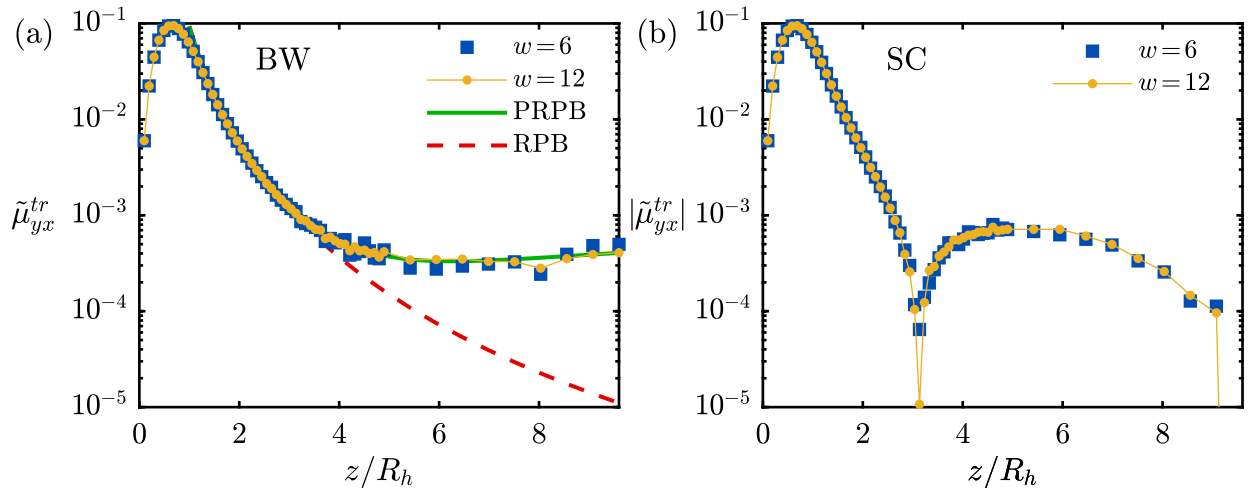


FIG. 5. Normalized translation-rotation self mobility, $\tilde{\mu}_{yx}^{tr} = (6\pi\eta R_h^2) \mu_{yx}^{tr}$, above the lower wall ($z \in [0, \frac{1}{2}H]$) in the BW and SC geometries for $w = 6$ and $w = 12$ (a doubly-refined grid). For the BW geometry, we also show the results from PRPB and the half-space *non-periodized* RPB tensors. Although not shown in this figure, for both BW and SC geometries, we find that the symmetric analog μ_{xy}^{rt} agrees with μ_{yx}^{tr} well within five digits. For the SC geometry, we show the absolute value due to a sign change for $z \gtrsim 3R_h$.

results for $w = 6$, and to less extent, even a doubly refined result with $w = 12$, exhibit small numerical oscillations as the particle moves away from the wall.

To understand this behavior, consider the analytical form of μ_{yx}^{tr} (from the RPB tensor) for two particles, far away from each other, at the same height z ,

$$\eta\mu_{yx}^{tr}(z) \approx \frac{1}{6\pi} \frac{3\hat{r}_z(\hat{r}_x)^2}{\|\mathbf{r}\|^2}, \quad (59)$$

where

$$\mathbf{r} = [x^{(1)} - x^{(2)} \quad y^{(1)} - y^{(2)} \quad 2z], \quad \hat{\mathbf{r}} = \frac{\mathbf{r}}{\|\mathbf{r}\|}. \quad (60)$$

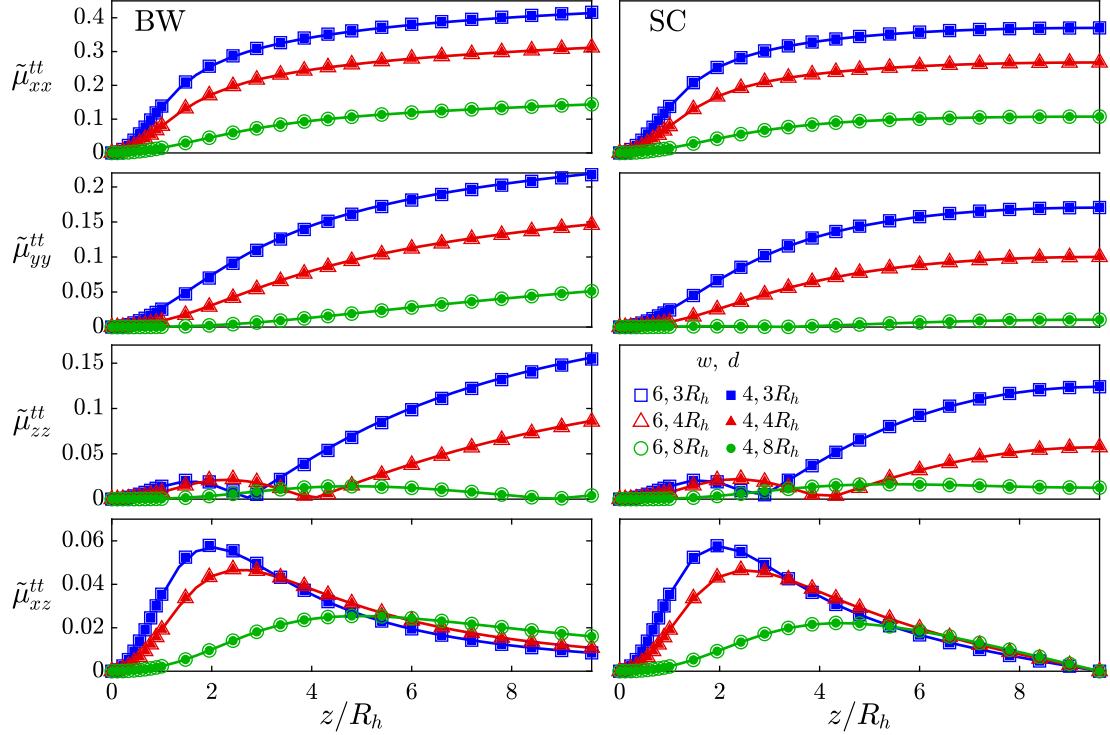


FIG. 6. Normalized translation-translation pair mobility, $\tilde{\mu}^{tt} = (6\pi\eta R_h) \mu^{tt}$, above the lower wall ($z \in [0, \frac{1}{2}H]$) in the BW (left panel) and SC (right panel) geometries, for a pair of particles at the same y and z , and distance $d = 3R_h, 4R_h, 8R_h$ away from each other along the x direction. Our results using the ES kernel are shown with empty and filled markers for $w = 6$ and $w = 4$, respectively. The reference results, PRPB for the BW geometry, and $w = 12$ for the SC geometry, are solid curves.

We can approximate the sum of the RHS of (59) over the periodic images in the xy plane with an integral in polar coordinates. We find that as $z \rightarrow \infty$, the approximate sum converges to a constant $\sim L^{-2}$, and for $z \ll L$, it is $\sim z/L^3$. The self term decays like R_h^2/z^4 . Therefore, the combined mobility (self plus images) is dominated by the self term for small z and by the images for large z . This results in a minimum in $\mu_{yx}^{tr}(z)$, at roughly $z_{\min} \sim (L^3 R_h^2)^{1/5}$, followed by a plateau. If the particle goes above z_{\min} , the translation-rotation self coupling is dominated by the periodic images.

For the slit channel, symmetry is always broken by the presence of the upper and lower walls, except at the exact center of the channel $z/R_h = H/2$. That is, $\mu_{yx}^{tr}(H/2) = 0$, and we exclude this point from our plot due to the log scale on the y axis. As expected, we have similar behavior between SC and BW near the wall, and the numerical oscillations are diminished for both the $w = 6$ and $w = 12$ reference computation in the SC geometry. Interestingly, there is a sign change in μ_{yx}^{tr} in the slit channel for $z \gtrsim 3R_h$ (likely due to periodic images), although the coupling is weak.

B. Pair mobility

Because we use a non-Gaussian tensor product kernel (53), the pair mobility for two blobs in an unbounded domain does not have a strictly isotropic form, even in the absence of discretization errors, and, furthermore, the pair mobility is difficult to compute analytically. In Appendix B we examine the pair mobility in the absence of walls numerically using a (large) TP domain. Our main conclusion is that the results obtained with the ES kernel are within a percent of those for a Gaussian kernel, and are isotropic to an accuracy of at least two digits for the kernel and grid choices we selected.

Here we briefly investigate the behavior of the linear and rotational relative mobility of pairs of identical particles at the same height z above the wall, separated by a distance $d = 3R_h, 4R_h, 8R_h$ in the x direction.

First, we examine the pair-wise components of \mathcal{M}^{tt} in Fig. 6. All numerical results compare well to the reference results, i.e., PRPB in BW geometry, and a doubly-refined result in SC geometry, for both $w = 4$ and $w = 6$. For each mobility component considered, we see that when the particles are near the wall, greater separation leads to reduced

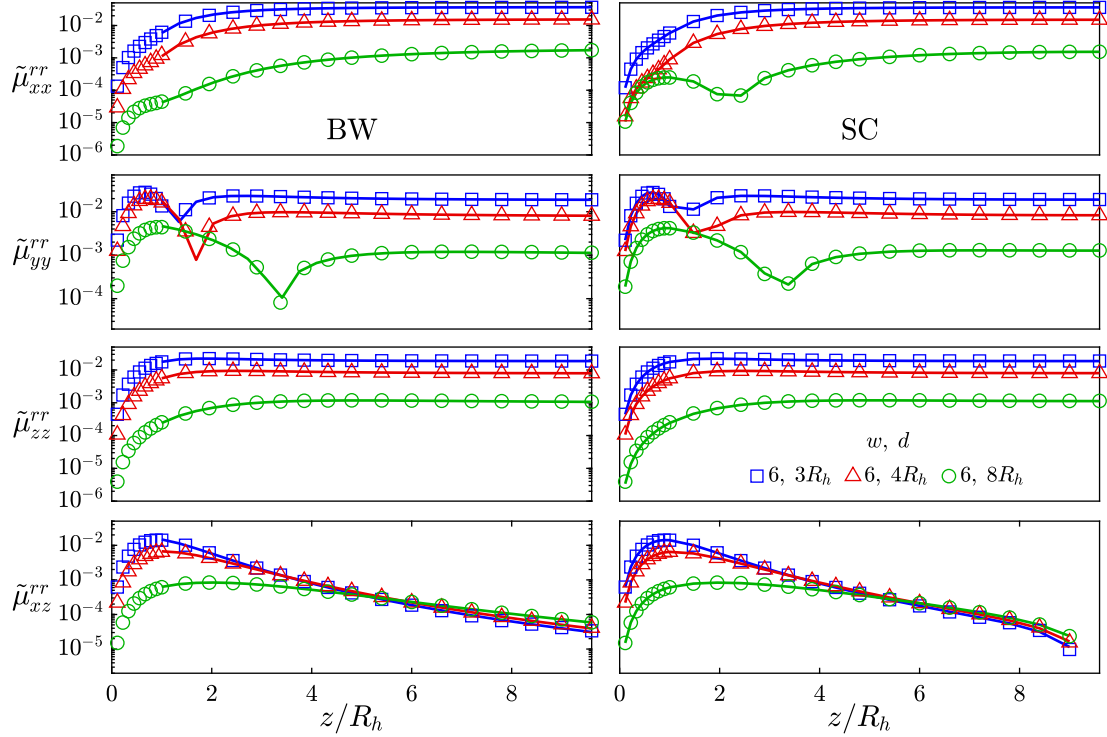


FIG. 7. Normalized rotation-rotation pair mobility, $\tilde{\mu}^{rr} = (8\pi\eta R_h^3) \mu^{rr}$, for the same system as in Fig. 6. Our results using the ES kernel with $w = 6$ are shown with empty markers. The reference results, PRPB for the BW geometry, and $w = 12$ for the SC geometry, are solid curves. Note that μ_{xz}^{rr} goes to zero at the midplane due to symmetry.

magnitude of coupling. This is also the case further away from the bottom wall, except for μ_{xz}^{tt} . It is also interesting to note that in BW geometry, μ_{zz}^{tt} have local minima in the coupling when particles aren't overlapping the wall, and the z location of these minima increase with particle separation. In SC geometry, μ_{zz}^{tt} have similar minima pattern, but for $d = 8R_h$, we do not obtain a minimum.

In Fig. 7, we inspect the pair-wise components of \mathcal{M}^{rr} , μ_{yy}^{rr} , μ_{xx}^{rr} , μ_{xz}^{rr} , and μ_{zz}^{rr} . Our numerical results compare very well to the reference results in either geometry, despite the weakness of the coupling. As for translation-translation, the coupling decreases with particle separation, except in the case of the perpendicular-parallel component μ_{xz}^{rr} . There is a similar minima pattern for μ_{yy}^{rr} when particles are not overlapping the wall, analogous to that observed for μ_{zz}^{tt} in Fig. 6. While the mobilities behave similarly in both SC and BW, we actually see a local minimum in μ_{xx}^{rr} in SC for $d = 8R_h$.

Lastly, in Fig. 8, we consider the pair-wise components of \mathcal{M}^{tr} , μ_{yz}^{tr} , μ_{yx}^{tr} , μ_{xy}^{tr} , and μ_{zy}^{tr} , and see that the reference results compare well to our numerical results. We highlight the same effects due to periodicity in xy as seen in Fig. 5 through the non-periodized RPB kernel (dotted lines) for μ_{yx}^{tr} and μ_{xy}^{tr} . That is, both μ_{yx}^{tr} and μ_{xy}^{tr} decay in a half-space as the particles are further from the bottom wall, but the periodicity in xy leads to a plateau in the mobility. For μ_{yx}^{tr} in SC, we see local minima when the particles are not touching the wall at $d = 3R_h, 4R_h$, but not $d = 8R_h$. Also in SC, we see μ_{xy}^{tr} for $d = 3R_h$ has a local minimum not observed for the other two separation distances. In both BW and SC geometries, we see a minimum in μ_{zy}^{tr} , with the position of the minima increasing in z with particle separation.

V. COLLOIDAL MONOLAYERS

We apply our method to a case study of a driven dense suspensions of colloidal microrollers near a bottom wall/floor, as recently investigated by Sprinkle et al. [21]. In this system, magnetic spherical colloidal particles sediment into a dense monolayer near a bottom wall. A magnetic field is used to spin the particles with the axis of rotation parallel to the wall, which induces a translational motion of the particles along the wall due to the rotation-translation coupling induced by the presence of the floor. A collective active steady state is established, and experimental and numerical results provided by Sprinkle et al. [21] show the existence of two layers of rollers, a slower layer close to the wall, and a faster layer above the slow one. Since the colloidal layer remains close to the wall in the z direction but extends far

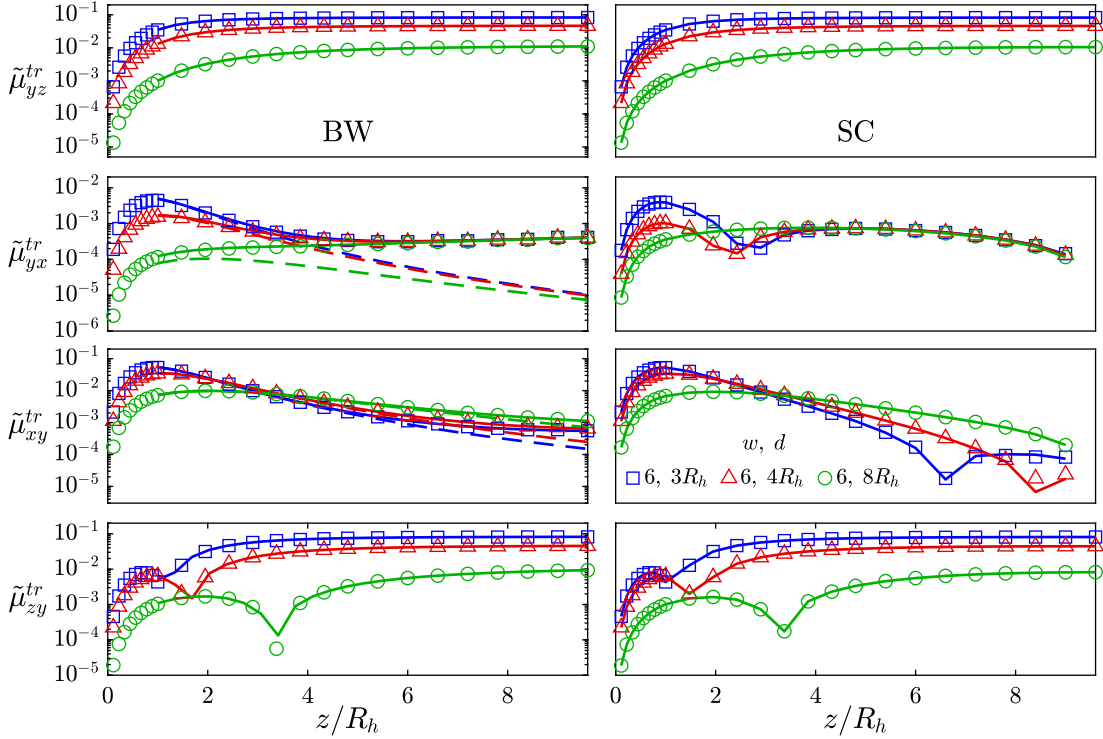


FIG. 8. Normalized translation-rotation pair mobility, $\tilde{\mu}^{tr} = (6\pi\eta R_h^2) \mu^{tr}$, for the same system and labels as in Fig. 7. The half-space non-periodized RPB is also shown for mobility components μ_{yx}^{tr} and μ_{xy}^{tr} in BW as dashed curves. Although not shown here, for both BW and SC geometries, we find that the symmetric components in \mathcal{M}^{rt} agree with each other to well within five digits at each height. Note that the yx , xy , and zy components of μ^{tr} go to zero at the midplane due to symmetry.

in the xy directions, this system is an ideal target for our doubly-periodic solver.

In [21], some of us developed a lubrication-corrected variant of Stokesian Dynamics method (without stresslet corrections) to simulate the collective driven dynamics, and found good agreements between computational and experimental results. In these prior studies, we computed the far-field hydrodynamic interactions using a GPU-accelerated direct pairwise summation of the Rotne-Prager-Blake tensor [22] generalized to account for torques/rotation. To approximate the doubly-periodic conditions, in these prior works [33], each particle interacted only with $3 \times 3 = 9$ periodic copies of every other particle. Because of the quadratic scaling of the direct summation, this increased the cost of the calculation by as much as two orders of magnitude (i.e., a factor of $9^2 = 81$), severely limiting scalability to larger numbers of particles.

In this section we apply our linearly-scaling method to the same problem. First, we validate the linear scaling of our method up to the memory limitations on the GPU by periodically replicating a representative configuration from the steady state conditions found numerically in [21]. We then study the convergence of an iterative method to compute the (far-field) Brownian (stochastic) particle displacements, as efficient and (log-)linear-scaling dynamic simulations require rapid convergence of the iterative method with a number of iterations independent of the number of particles. While we have previously established this for bottom wall geometries [33], here we confirm this to be the case also in slit channel geometries, despite the slower decay of the hydrodynamic interactions with particle distance.

A. Linear scaling

In this section, we demonstrate the linear scaling of our GPU-based solver with the number of particles. Figure 9 shows the computation time as we periodically replicate a representative configuration of $N = 2048$ particles [21] in the xy plane direction to increase the number of particles. The original configuration before replication has a system size $L_{x/y} = L = 128.8R_h$ and $H \approx 9R_h$ (see Table III). We test here scaling for the case when there are only forces applied (M , monopole-only, kernel width $w = 4$), and when both forces and torques are applied ($M \& D$, monopole and dipole terms, kernel width $w = 6$). The computational cost for the dipole case is significantly larger than the monopole-only case, primarily because a larger grid size is required for kernel width $w = 6$, and because additional FFTs are required in the present implementation of spreading and interpolation for the dipole terms. For

the monopole-only case, the biggest system has $L = 18 \times 128.8R_h = 2318.4R_h$ (H remains the same) and contains 663552 particles, the maximum size that fits in the 32GB of memory in a V100 GPU. After 169 replicas (346112 particles) the 12GB of memory available in the Titan V GPU are not enough.

TABLE III. Simulation parameters for the performance tests when only forces are applied (monopole-only, M), and when both forces and torques are applied (monopole and dipole, M & D).

	H	$L_{x/y}$	N_z	$N_{x/y}$	w_M	β_M/w_M	w_D	β_D/w_D
M	$9.1R_h$	$128.8R_h$	19	150	4	1.87		
M & D	$9.2R_h$	$128.8R_h$	26	216	6	1.38	6	2.3

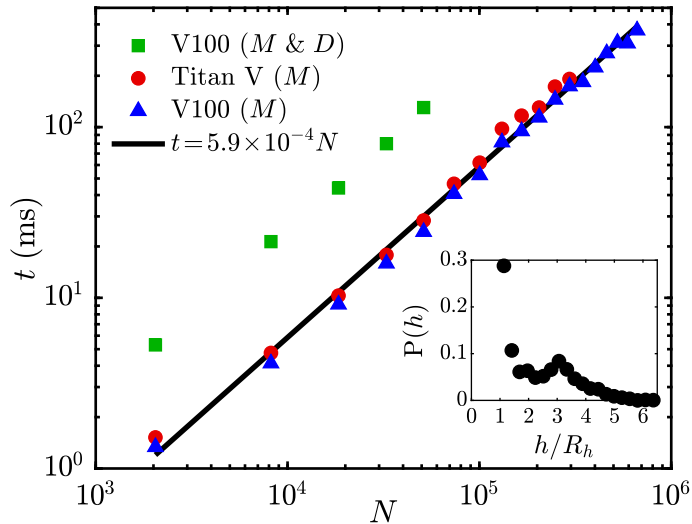


FIG. 9. Time per mobility solve versus number of particles with parameters given in Table III, on V100 and Titan V NVIDIA GPUs. We replicate a system of 2048 particles in the xy plane. Particles are uniformly distributed in the planar direction, with an area packing fraction of $\phi = 0.4$, and a bimodal (two-layer) distribution of heights h above the wall, as shown in the inset. The biggest system contains 663552 particles and takes 368 ms to compute with UAMMD on a V100 GPU.

Our performance test results clearly shows a linear scaling with the number of particles, allowing computations with on the order of a million particles in less than a second. This is a significant improvement over the direct summation method used by Sprinkle et al. [21]. It is difficult to perform direct timing comparisons with the linear-scaling, FMM-based STKFMM, multicore code of Wen et al. [26, 27], since the performance of this CPU-based code depends heavily on the type of supercomputer and number of cores used, and optimization options. Nevertheless, rough timing comparisons suggest our simple GPU-friendly Stokes solver is at least an order of magnitude faster on this example for standard workstations.

B. Lanczos convergence

Brownian Dynamics simulations require a method to generate Brownian particle “velocities,” Gaussian random variables with mean zero and covariance $\sim \mathcal{M}$, i.e., $\mathbf{g} = \mathcal{M}^{\frac{1}{2}}\mathcal{W}$, where $\mathcal{M}^{\frac{1}{2}}$ is the mobility matrix square root and \mathcal{W} is a collection of independent identically distributed (i.i.d) random numbers with zero mean and unit standard deviation. Lanczos iterative algorithm [35] can be used to estimate \mathbf{g} in Krylov subspace. Prior work has shown that the number of iterations required to achieve a certain tolerance is independent of the number of particles in suspensions of particles near a single wall (BW geometry) due to the hydrodynamic screening of the wall (see Fig. 1 in [33]), but grows with the number of particles in the absence of a wall (in a TP environment [24]; also see the inset of Fig. 1 in [33]).

One could assume that the convergence rate of the Lanczos algorithm depends on how fast the hydrodynamic interactions decay with distance. In particular, we expect that the number of iterations is controlled by the slowest

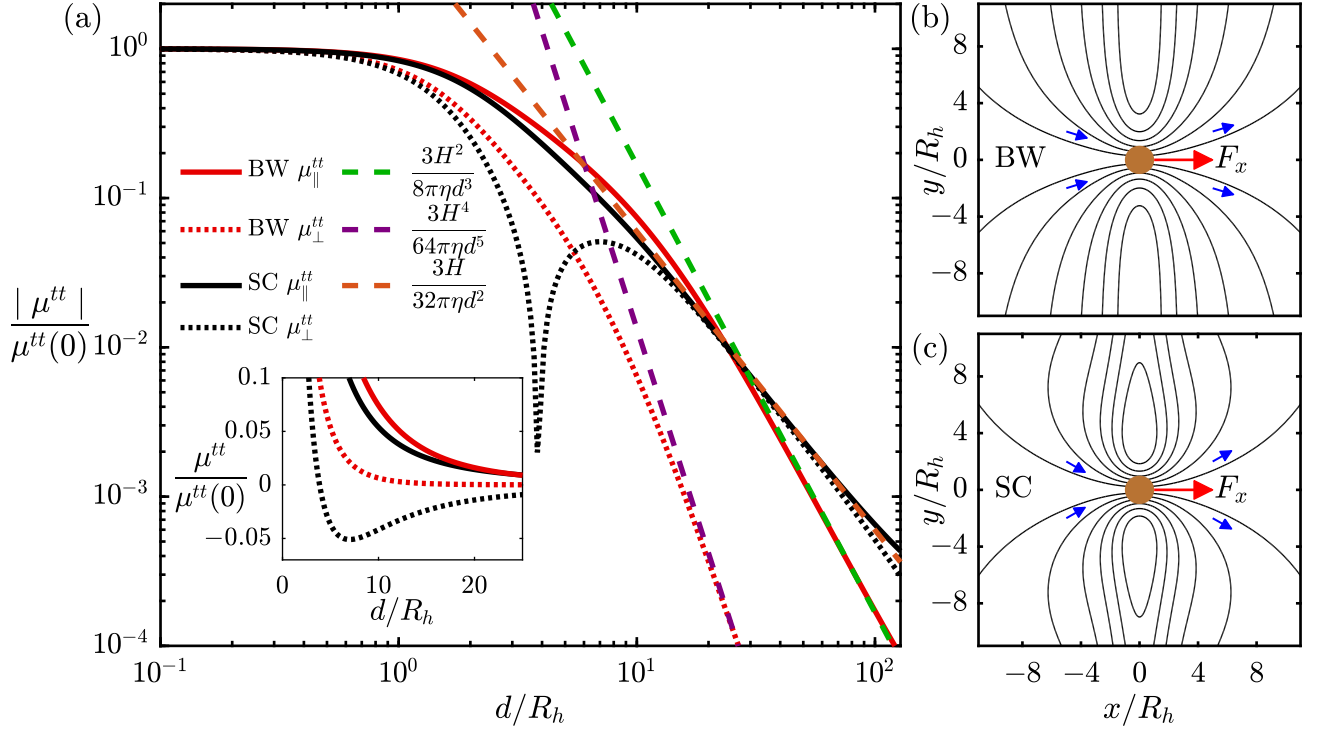


FIG. 10. (a) Two particles are placed at the same height $z = \frac{1}{2}H$, same y , and a distance d apart from each other along the x direction. One is pulled with a force in the x or y direction and the induced mobility on the other particle is measured in, respectively, x (parallel component, $\mu_{\parallel}^{tt} = \mu_{xx}^{tt}$) and y (perpendicular component, $\mu_{\perp}^{tt} = \mu_{yy}^{tt}$) directions. The dashed lines correspond to theoretical asymptotes for $d \gg R_h$. (b, c) Streamlines of a ghost particle velocity about a particle being pulled along the x direction with a force F_x . Streamlines are calculated using the x and y velocity components $U_x^{(2)} = \mu_{xx}^{tt} F_x$ and $U_y^{(2)} = \mu_{yy}^{tt} F_x$. Parameters: $L = 512R_h$, $H = 8R_h$, $w = 6$, $\eta = 1$, $R_h = 1$.

decaying hydrodynamic interactions. Therefore, for our problem of monolayers, we focus on the translation-translation components of the hydrodynamic interactions (no torques) in the xy plane, for which the decay occurs relatively slower. Let us consider a pair of particles located at the same height $z = \frac{1}{2}H$, same y , and distance d away from each other in the x direction. We apply a unit force on one of the particles in either x or y directions and measure the resulting translational velocity of the other one in the same direction (i.e., μ_{xx}^{tt} and μ_{yy}^{tt} which we refer to as parallel, μ_{\parallel}^{tt} , and perpendicular, μ_{\perp}^{tt} , mobility components) (cf. Fig. 10(a)). We compare our results to the available asymptotic formulas in the literature for $d \gg R_h$. For SC geometry, both parallel and perpendicular mobilities approach the same asymptote $3H/(32\pi\eta d^2)$ (see Eq. (51) in [43]). For BW geometry, the parallel and perpendicular mobilities approach the asymptotes $3H^2/(8\pi\eta d^3)$ and $3H^4/(64\pi\eta d^5)$, respectively [25]. Also, note that the data is normalized with the corresponding $\mu^{tt}(d \rightarrow 0)$, which is the mobility of a single particle located at height $z = \frac{1}{2}H$. (For large values of H and in the absence of periodic effects, $\mu^{tt}(d \rightarrow 0)$ approaches the mobility of a particle in an unbounded domain, $1/(6\pi\eta R_h)$.)

An interesting observation is that μ_{\perp}^{tt} becomes negative (presence of backflow) for $d/R_h \gtrsim 4$ in the SC geometry (see inset of Fig. 10(a)). To provide a better picture of the this phenomena, in Figs. 10(b) and (c) we show representative streamlines of a ghost particle velocity near a particle that is being dragged along the x direction. We clearly see the existence of fluid vortices in the SC geometry case. Another important, and counter-intuitive, point is that the SC geometry shows a slower decay rate compared to the BW geometry [1]. Such a slow decay warrants an accurate analysis of the Lanczos convergence rate in the SC geometry and how it compares with that in the BW and TP geometries.

Figure 11 shows the relative difference $\epsilon_m = \|\mathbf{g}_m - \mathbf{g}_{m-1}\|/\|\mathbf{g}_{m-1}\|$ of the Lanczos algorithm versus the number of iterations m in the BW, SC, and TP geometries. For the BW geometry, we observe the same phenomenon showcased in [33], where the hydrodynamic screening of the wall makes the convergence of the Lanczos algorithm essentially independent of the number of particles. The number of iterations required to achieve a 3-digit accuracy remains less than 10 for $N = 2^{11}$ to 2^{17} particles. Surprisingly, the SC geometry shows even a faster convergence rate, despite the

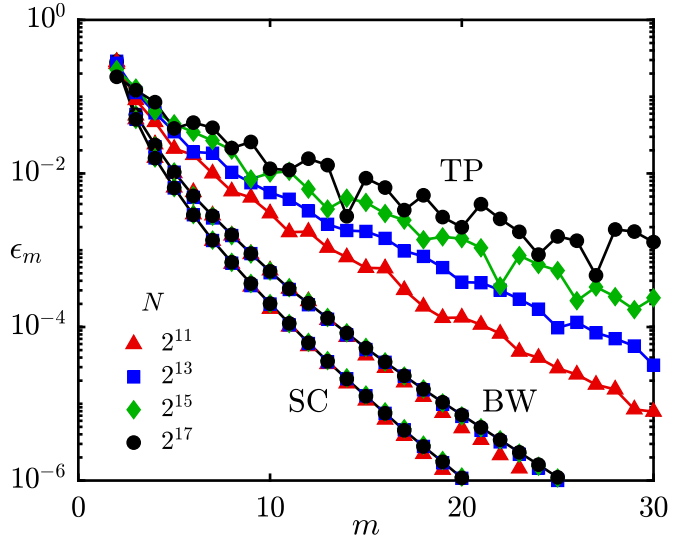


FIG. 11. Relative error ϵ_m vs number of iterations m of the Lanczos algorithm for a suspension of particles with the same configuration as in Fig. 9. Similar to Fig. 9, the system is replicated in the plane direction to study higher particle counts. The results for BW and SC geometries are obtained with the parameters given in Table III but $H = 7.5R_h$. The TP result is for the same configuration but in triply-periodic mode, where we set the height of the (periodic) domain to $H = 130R_h$.

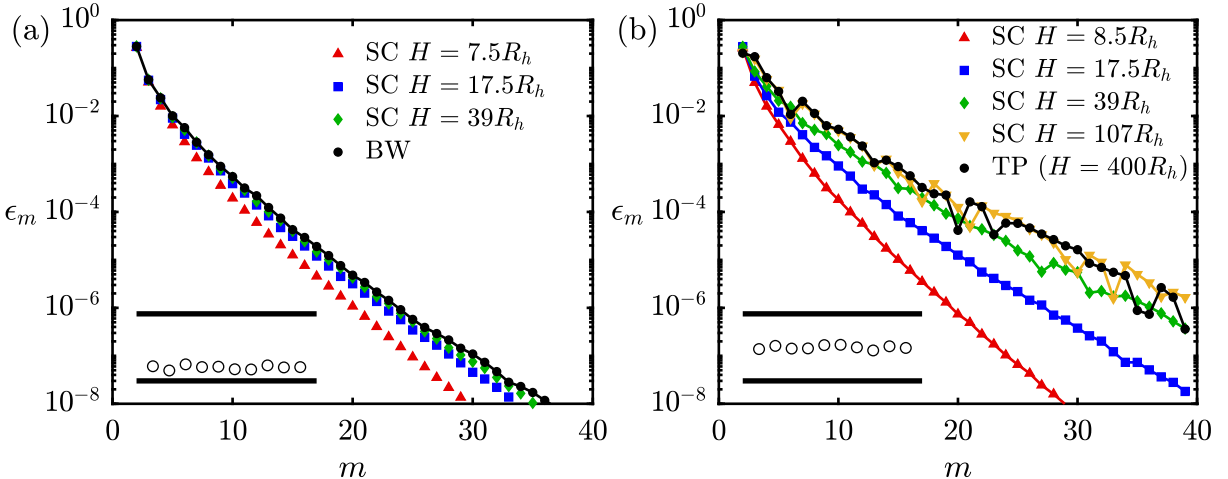


FIG. 12. Lanczos convergence for a slit channel with increasing gap H , in two scenarios: (a) Particles ($N = 2048$) are kept near the bottom wall and H increases (which becomes increasingly similar to the bottom wall geometry); (b) Particles are kept at the middle of the channel and H increases (which becomes increasingly similar to a TP geometry with $H \rightarrow \infty$). Although not shown, above a relative error of $\sim 10^{-6}$ the convergence is not affected by the floating point precision (single or double precision).

slower decay rate of the pair mobilities in this geometry (cf. Fig. 10). Perhaps this can be explained by the fact that the slowly decaying component is *not* of hydrodynamic origin, but rather comes from incompressibility; the actual hydrodynamic interactions are exponentially screened in the SC geometry [1]. Finally, consistent with prior work [24], the convergence rate drops significantly (and fails at times) for large TP systems due to the absence of the wall effects.

It should be noted that the convergence behavior for the SC geometry depends heavily on the gap size and the particle height, as we explore Fig. 12. We first place 2048 particles near the bottom wall and increase the gap H between the two walls (cf. Fig. 12(a)). We observe that as $H \rightarrow \infty$, the SC behavior approaches that of a BW geometry. We repeat this experiment with the particles placed at the midplane (cf. Fig. 12(b)). This time, as $H \rightarrow \infty$, the system behavior approaches that of a TP system, as expected.

Appendix A: Slit channel geometry with slip velocity

For the SC geometry, for increased generality and because of its relevance to microfluidics, we impose partial slip boundary conditions at $z = 0$ and $z = H$:

$$\mathbf{u}|_{z=0} - \mathbf{u}_0^{\text{wall}} = \ell_0 \begin{bmatrix} \frac{\partial u(x, y, 0)}{\partial z} & \frac{\partial v(x, y, 0)}{\partial z} & 0 \end{bmatrix}, \quad (\text{A1a})$$

$$\mathbf{u}|_{z=H} - \mathbf{u}_H^{\text{wall}} = -\ell_H \begin{bmatrix} \frac{\partial u(x, y, H)}{\partial z} & \frac{\partial v(x, y, H)}{\partial z} & 0 \end{bmatrix}. \quad (\text{A1b})$$

Here, $\mathbf{u}_{0/H}^{\text{wall}} = \begin{bmatrix} u_{0/H}^{\text{wall}} & v_{0/H}^{\text{wall}} & 0 \end{bmatrix}$ are the wall velocities, and $\ell_{0/H}$ are the slip lengths, with $\ell = 0$ denoting a no-slip wall.

For simplicity, we only write explicitly equations for u , with identical equations for v with the swap $x \leftrightarrow y$. Note that the DP solver remains the same as that of the single wall geometry, noting that particle kernels have images in both walls. It is the correction solve that takes care of the boundary conditions.

1. Correction Solve

We have $\mathbf{u} = \mathbf{u}_{\text{DP}} + \mathbf{u}_{\text{corr}}$, which upon substitution into (A1), and some rearrangement, yields

$$\mathbf{u}_{\text{corr}}|_{z=0} - \ell_0 \begin{bmatrix} \frac{\partial u_{\text{corr}}(x, y, 0)}{\partial z} & \frac{\partial v_{\text{corr}}(x, y, 0)}{\partial z} & 0 \end{bmatrix} = [u_0(x, y) \ v_0(x, y) \ w_0(x, y)], \quad (\text{A2a})$$

$$\mathbf{u}_{\text{corr}}|_{z=H} + \ell_H \begin{bmatrix} \frac{\partial u_{\text{corr}}(x, y, H)}{\partial z} & \frac{\partial v_{\text{corr}}(x, y, H)}{\partial z} & 0 \end{bmatrix} = [u_H(x, y) \ v_H(x, y) \ w_H(x, y)], \quad (\text{A2b})$$

where,

$$u_0(x, y) = u_0^{\text{wall}} - u_{\text{DP}}(x, y, 0) + \ell_0 \frac{\partial u_{\text{DP}}(x, y, 0)}{\partial z}, \quad (\text{A3a})$$

$$w_0(x, y) = -w_{\text{DP}}(x, y, 0), \quad (\text{A3b})$$

$$u_H(x, y) = u_H^{\text{wall}} - u_{\text{DP}}(x, y, H) - \ell_H \frac{\partial u_{\text{DP}}(x, y, H)}{\partial z}, \quad (\text{A3c})$$

$$w_H(x, y) = -w_{\text{DP}}(x, y, H). \quad (\text{A3d})$$

Following a similar method as the one described in Sec. III B, one can find the general solutions to \hat{p}_{corr} and $\hat{\mathbf{u}}_{\text{corr}}$, the pressure and velocity in Fourier space, as

$$\hat{p}_{\text{corr}}(\mathbf{k}, z) = C_0 e^{-kz} + D_0 e^{kz}, \quad (\text{A4})$$

$$\hat{u}_{\text{corr}}(\mathbf{k}, z) = -\frac{C_0 i k_x}{2\eta k} z e^{-kz} + \frac{D_0 i k_x}{2\eta k} z e^{kz} + C_x e^{-kz} + D_x e^{kz}, \quad (\text{A5})$$

$$\hat{w}_{\text{corr}}(\mathbf{k}, z) = \frac{C_0}{2\eta} z e^{-kz} + \frac{D_0}{2\eta} z e^{kz} + C_z e^{-kz} + D_z e^{kz}. \quad (\text{A6})$$

To find the constants, we start by writing the boundary conditions (A2) in Fourier space:

$$\hat{u}_{\text{corr}}(\mathbf{k}, 0) - \ell_0 \frac{\partial \hat{u}_{\text{corr}}(\mathbf{k}, 0)}{\partial z} = \hat{u}_0(\mathbf{k}), \quad (\text{A7a})$$

$$\hat{w}_{\text{corr}}(\mathbf{k}, 0) = \hat{w}_0(\mathbf{k}), \quad (\text{A7b})$$

$$\hat{u}_{\text{corr}}(\mathbf{k}, H) + \ell_H \frac{\partial \hat{u}_{\text{corr}}(\mathbf{k}, H)}{\partial z} = \hat{u}_H(\mathbf{k}), \quad (\text{A7c})$$

$$\hat{w}_{\text{corr}}(\mathbf{k}, H) = \hat{w}_H(\mathbf{k}). \quad (\text{A7d})$$

Substituting (A5) and (A6) into (A7) results in the following equations for the unknown constants

$$\left(\frac{ik_x \ell_0}{2\eta k} \right) C_0 - \left(\frac{ik_x \ell_0}{2\eta k} \right) D_0 + (1 + k\ell_0) C_x + (1 - k\ell_0) D_x = \hat{u}_0(\mathbf{k}), \quad (\text{A8a})$$

$$C_z + D_z = \hat{w}_0(\mathbf{k}), \quad (\text{A8b})$$

$$\frac{ik_x H e^{-kH}}{2\eta k} \left(k\ell_H - \frac{\ell_H}{H} - 1 \right) C_0 + \frac{ik_x H e^{kH}}{2\eta k} \left(k\ell_H + \frac{\ell_H}{H} + 1 \right) D_0 + e^{-kH} (1 - k\ell_H) C_x + e^{kH} (1 + k\ell_H) D_x = \hat{u}_H(\mathbf{k}), \quad (\text{A8c})$$

$$\frac{H e^{-kH}}{2\eta} C_0 + \frac{H e^{kH}}{2\eta} D_0 + e^{-kH} C_z + e^{kH} D_z = \hat{w}_H(\mathbf{k}). \quad (\text{A8d})$$

Furthermore, the continuity equation in Fourier space (38) can be written at $z = 0, H$:

$$ik_x \hat{u}_{\text{corr}}(\mathbf{k}, 0/H) + ik_y \hat{v}_{\text{corr}}(\mathbf{k}, 0/H) + \frac{\partial \hat{w}_{\text{corr}}(\mathbf{k}, 0/H)}{\partial z} = 0. \quad (\text{A9})$$

Inserting the general solutions (A5)–(A6) into the above equations yields two more equations for the unknown coefficients:

$$\frac{C_0}{2\eta} + \frac{D_0}{2\eta} + ik_x C_x + ik_x D_x + ik_y C_y + ik_y D_y - k C_z + k D_z = 0, \quad (\text{A10a})$$

$$\frac{e^{-kH}}{2\eta} C_0 + \frac{e^{kH}}{2\eta} D_0 + ik_x e^{-kH} C_x + ik_x e^{kH} D_x + ik_y e^{-kH} C_y + ik_y e^{kH} D_y - k e^{-kH} C_z + k e^{kH} D_z = 0. \quad (\text{A10b})$$

Now we have a system of eight equations given by (A8) (with the corresponding equations for v) and (A10) which can be solved to find the eight unknown constants $C_0, D_0, C_{x/y/z}, D_{x/y/z}$ for each $\mathbf{k} = [k_x \ k_y] \neq \mathbf{0}$.

2. Zero mode ($\mathbf{k} = \mathbf{0}$)

The zero mode $\mathbf{k} = \mathbf{0}$ solutions to the velocity component normal to the walls, $\hat{w}(\mathbf{0}, z)$, and the pressure, $\hat{p}(\mathbf{0}, z)$, remain the same as those of the single wall geometry, given by (50) and (47).

However, the $\mathbf{k} = \mathbf{0}$ mode of the tangential velocity components will be different. Fourier transform of the slip boundary conditions (A1) is

$$\hat{\mathbf{u}}(\mathbf{k}, 0) - \hat{\mathbf{u}}_0^{\text{wall}}(\mathbf{k}) = \ell_0 \begin{bmatrix} \frac{\partial \hat{u}(\mathbf{k}, 0)}{\partial z} & \frac{\partial \hat{v}(\mathbf{k}, 0)}{\partial z} & 0 \end{bmatrix}, \quad (\text{A11a})$$

$$\hat{\mathbf{u}}(\mathbf{k}, H) - \hat{\mathbf{u}}_H^{\text{wall}}(\mathbf{k}) = -\ell_H \begin{bmatrix} \frac{\partial \hat{u}(\mathbf{k}, H)}{\partial z} & \frac{\partial \hat{v}(\mathbf{k}, H)}{\partial z} & 0 \end{bmatrix}. \quad (\text{A11b})$$

Therefore, similar to the single-wall case (cf. (51) and (52)), one can find $\hat{u}(\mathbf{0}, z)$ (and analogously $\hat{v}(\mathbf{0}, z)$) via solving the following BVPs:

$$\frac{\partial^2 \hat{u}(\mathbf{0}, z)}{\partial z^2} = -\frac{\hat{f}(\mathbf{0}, z)}{\eta}, \quad \hat{u}(\mathbf{0}, 0) - \ell_0 \frac{\partial \hat{u}(\mathbf{0}, 0)}{\partial z} = \hat{u}_0^{\text{wall}}(\mathbf{0}), \quad \hat{u}(\mathbf{0}, H) + \ell_H \frac{\partial \hat{u}(\mathbf{0}, H)}{\partial z} = \hat{u}_H^{\text{wall}}(\mathbf{0}). \quad (\text{A12})$$

Appendix B: Translation-translation pair coupling in a triply periodic domain

In this Appendix, we numerically compute and investigate the invariance under rotation and translation of the pair translational mobility, \mathcal{M}^{tt} , for the ES kernel in a triply periodic domain. We will examine our numerical approximation to \mathcal{M}^{tt} as a function of $d = \|\mathbf{d}\| = \|\mathbf{d}^{(1)} - \mathbf{d}^{(2)}\|$, where $\mathbf{d}^{(1)}$ and $\mathbf{d}^{(2)}$ are the positions of the two particles. If the kernel is rotationally invariant (which our tensor product ES kernel (53) is not), then \mathcal{M}^{tt} would have the invariant form

$$\mathcal{M}^{tt}(\mathbf{d}) = f(d) \mathcal{I} + g(d) \frac{\mathbf{d} \otimes \mathbf{d}}{d^2}, \quad (\text{B1})$$

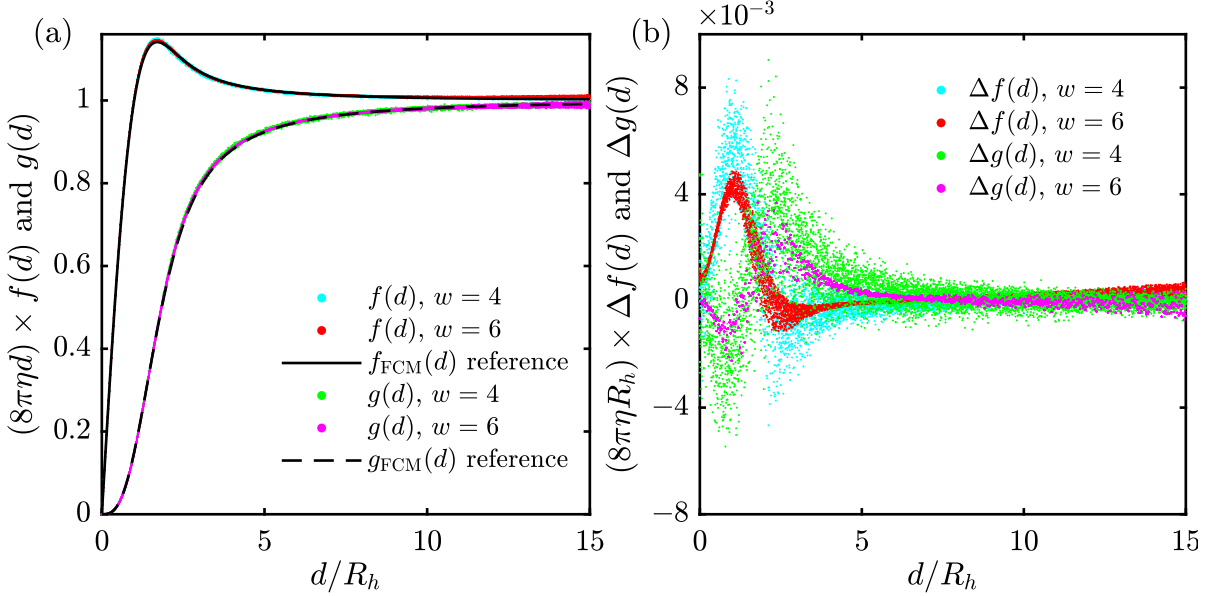


FIG. B1. (a) Numerically calculated, normalized, mobility functions $(8\pi\eta d)f(d)$ and $(8\pi\eta d)g(d)$, for two spheres in a large triply-periodic domain with ES kernel, versus the distance d between the two spheres, along with reference FCM curves given by (B2) for the continuum model in free space with Gaussian envelopes. (b) Normalized difference between the numerical and analytical values of $f(d)$ and $g(d)$ (i.e., $(8\pi\eta R_h)[f(d) - f_{\text{FCM}}(d)]$ and $(8\pi\eta R_h)[g(d) - g_{\text{FCM}}(d)]$, respectively) versus d .

for some functions $f(d)$ and $g(d)$. Lomholt and Maxey [6] derived analytical forms for *free space* $f(d)$ and $g(d)$ when particles are represented by Gaussian force envelopes (in the continuum),

$$f(d) = \frac{1}{8\pi\eta d} \left(\left(1 + 2\frac{R_h^2}{\pi d^2} \right) \text{erf} \left(\frac{d\sqrt{\pi}}{2R_h} \right) - 2\frac{R_h}{\pi d} \exp \left(-\frac{\pi d^2}{4R_h^2} \right) \right) \quad (\text{B2a})$$

$$g(d) = \frac{1}{8\pi\eta d} \left(\left(1 - 6\frac{R_h^2}{\pi d^2} \right) \text{erf} \left(\frac{d\sqrt{\pi}}{2R_h} \right) + 6\frac{R_h}{\pi d} \exp \left(-\frac{\pi d^2}{4R_h^2} \right) \right), \quad (\text{B2b})$$

The invariant form (B1) does not strictly apply in practice for our FCM method for several reasons. The first is that the tensor product kernel we use is not rotationally invariant as a Gaussian kernel is. The second is that rotational invariance is broken for a finite system such as a periodic box. Lastly, there are discretization artifacts due to the finite grid resolution in the Stokes solver, especially for the small kernel widths like $w = 4$. Here we numerically demonstrate that our method produces a pair mobility that matches (B2) to at least two digits, at least for $d \ll L$.

The numerical domain is a cubic box of side length $L = 200$ and uniform grid spacing $h = 1$. We consider particles represented by the optimal $w = 6$ monopole kernel with $R_h = 1.55$, or the optimal $w = 4$ monopole kernel with $R_h = 1.205$ (cf. Table II). The two particles always use the same kernel types. We generate 10^4 random particle pair configurations a distance $d \in [0, 25]$ from each other. For each pair, we compute the pair parallel and perpendicular mobilities μ_{\parallel} and μ_{\perp} with respect to the direction \mathbf{p} . According to (B1), we have

$$\mu_{\parallel} \approx f(d; L) + g(d), \quad (\text{B3})$$

$$\mu_{\perp} \approx f(d; L), \quad (\text{B4})$$

where $f(d; L)$ depends on L due to the finite size of the triply-periodic box. Following Hasimoto's corrections for the self mobility in triply periodic domains [41] (cf. (55)), we correct the numerically calculated $f(d; L)$ for $d \ll L$ by

$$f(d) \approx f(d; L) + \frac{1}{6\pi\eta R_h} \left(2.84 \frac{R_h}{L} \right). \quad (\text{B5})$$

In Fig. B1, we compare the corrected $f(d)$ in (B5) and $g(d)$ for the ES kernel to the free space $f(d)$ and $g(d)$ for Gaussian force envelopes given by (B2). We see a good match for both $w = 4$ and $w = 6$ monopole ES kernels (cf. Fig. B1(a)). Fig. B1(b) shows the normalized difference between the numerically calculated $f(d)$ and $g(d)$ by the ES kernel and the traditional FCM mobility functions (B2). We see that the data clusters around a curve that is

systematically different from (B2), but the difference is on the order of a percent or less. Also, the scatter of $f(d)$ and $g(d)$ due to imperfect translational and rotational invariance are well controlled within two digits. Note that the increased error at high d/R_h is due to periodic boundary conditions artifact.

[1] H. Diamant, Hydrodynamic interaction in confined geometries, *Journal of the Physical Society of Japan* **78**, 041002 (2009).

[2] H. Yamakawa, Transport properties of polymer chains in dilute solution: Hydrodynamic interaction, *J. Chem. Phys.* **53**, 436 (1970).

[3] J. Rotne and S. Prager, Variational treatment of hydrodynamic interaction in polymers, *J. Chem. Phys.* **50**, 4831 (1969).

[4] R. Cortez, L. Fauci, and A. Medovikov, The method of regularized Stokeslets in three dimensions: analysis, validation, and application to helical swimming, *Physics of Fluids* **17**, 031504 (2005).

[5] M. R. Maxey and B. K. Patel, Localized force representations for particles sedimenting in Stokes flow, *International Journal of Multiphase Flow* **27**, 1603 (2001).

[6] S. Lomholt and M. R. Maxey, Force-coupling method for particulate two-phase flow: Stokes flow, *J. Comp. Phys.* **184**, 381 (2003).

[7] K. Yeo and M. R. Maxey, Dynamics of concentrated suspensions of non-colloidal particles in Couette flow, *Journal of Fluid Mechanics* **649**, 205 (2010).

[8] E. E. Keaveny, Fluctuating force-coupling method for simulations of colloidal suspensions, *J. Comp. Phys.* **269**, 61 (2014).

[9] K. Yeo and M. R. Maxey, Simulation of concentrated suspensions using the force-coupling method, *Journal of Computational Physics* **229**, 2401 (2010).

[10] A. H. Barnett, J. Magland, and L. af Klinteberg, A parallel nonuniform Fast Fourier Transform library based on an “exponential of semicircle” kernel, *SIAM Journal on Scientific Computing* **41**, C479 (2019).

[11] C. S. Peskin, The immersed boundary method, *Acta Numerica* **11**, 479 (2002).

[12] O. Maxian, R. P. Peláez, L. Greengard, and A. Donev, A fast spectral method for electrostatics in doubly periodic slit channels, *J. Chem. Phys.* **154**, 204107 (2021).

[13] J. W. Swan and G. Wang, Rapid calculation of hydrodynamic and transport properties in concentrated solutions of colloidal particles and macromolecules, *Physics of Fluids* **28**, 011902 (2016).

[14] A. M. Fiore and J. W. Swan, Fast Stokesian Dynamics, *Journal of Fluid Mechanics* **878**, 544 (2019).

[15] J. W. Swan, J. F. Brady, R. S. Moore, *et al.*, Modeling hydrodynamic self-propulsion with Stokesian Dynamics. Or teaching Stokesian Dynamics to swim, *Physics of Fluids* **23**, 071901 (2011).

[16] F. Balboa Usabiaga, B. Kallelom, B. Delmotte, A. P. S. Bhalla, B. E. Griffith, and A. Donev, Hydrodynamics of suspensions of passive and active rigid particles: a rigid multiblob approach, *Communications in Applied Mathematics and Computational Science* **11**, 217 (2016), software available at <https://github.com/stochasticHydroTools/RigidMultiblobsWall>.

[17] B. Sprinkle, F. B. Usabiaga, N. A. Patankar, and A. Donev, Large scale Brownian dynamics of confined suspensions of rigid particles, *J. Chem. Phys.* **147**, 244103 (2017), software available at <https://github.com/stochasticHydroTools/RigidMultiblobsWall>.

[18] S. F. Schoeller, A. K. Townsend, T. A. Westwood, and E. E. Keaveny, Methods for suspensions of passive and active filaments, *Journal of Computational Physics* **424**, 109846 (2021).

[19] O. Maxian, B. Sprinkle, C. S. Peskin, and A. Donev, Hydrodynamics of a twisting, bending, inextensible fiber in Stokes flow, *Phys. Rev. Fluids* **7**, 074101 (2022).

[20] A. Sierou and J. F. Brady, Accelerated Stokesian Dynamics simulations, *J. Fluid Mech.* **448**, 115 (2001).

[21] B. Sprinkle, E. B. van der Wee, Y. Luo, M. Driscoll, and A. Donev, Driven dynamics in dense suspensions of microrollers, *Soft Matter* **16**, 7982 (2020).

[22] J. W. Swan and J. F. Brady, Simulation of hydrodynamically interacting particles near a no-slip boundary, *Physics of Fluids* **19**, 113306 (2007).

[23] E. Wajnryb, K. A. Mizerski, P. J. Zuk, and P. Szymczak, Generalization of the Rotne–Prager–Yamakawa mobility and shear disturbance tensors, *Journal of Fluid Mechanics* **731**, R3 (2013).

[24] A. M. Fiore, F. B. Usabiaga, A. Donev, and J. W. Swan, Rapid sampling of stochastic displacements in Brownian dynamics simulations, *J. Chem. Phys.* **146**, 124116 (2017), software available at <https://github.com/stochasticHydroTools/PSE>.

[25] J. R. Blake, A note on the image system for a Stokeslet in a no-slip boundary, in *Proc. Camb. Phil. Soc.*, Vol. 70 (Cambridge Univ Press, 1971) pp. 303–310.

[26] W. Yan and R. Blackwell, Kernel aggregated fast multipole method, *Advances in Computational Mathematics* **47**, 1 (2021).

[27] W. Yan and M. Shelley, Universal image systems for non-periodic and periodic Stokes flows above a no-slip wall, *Journal of Computational Physics* **375**, 263 (2018).

[28] S. Srinivasan and A. Tornberg, Fast Ewald summation for Green’s functions of Stokes flow in a half-space, *Research in the Mathematical Sciences* **5**, 35 (2018).

[29] S. Delong, F. B. Usabiaga, R. Delgado-Buscalioni, B. E. Griffith, and A. Donev, Brownian dynamics without Green’s functions, *J. Chem. Phys.* **140**, 134110 (2014), software available at <https://github.com/stochasticHydroTools/FIB>.

[30] Y. Bao, J. Kaye, and C. S. Peskin, A Gaussian-like immersed-boundary kernel with three continuous derivatives and improved translational invariance, *Journal of Computational Physics* **316**, 139 (2016), software and updated documentation available at <https://github.com/stochasticHydroTools/IBMethod>, including also a new 5-pt kernel with three continuous

derivatives.

- [31] D. R. Ladiges, A. Nonaka, K. Klymko, G. C. Moore, J. B. Bell, S. P. Carney, A. L. Garcia, S. R. Natesh, and A. Donev, Discrete ion stochastic continuum overdamped solvent algorithm for modeling electrolytes, *Phys. Rev. Fluids* **6**, 044309 (2021).
- [32] B. Kallemov, A. P. S. Bhalla, B. E. Griffith, and A. Donev, An immersed boundary method for rigid bodies, *Communications in Applied Mathematics and Computational Science* **11**, 79 (2016), software available at <https://github.com/stochasticHydroTools/RigidBodyIB>.
- [33] F. B. Usabiaga, B. Delmotte, and A. Donev, Brownian dynamics of confined suspensions of active microrollers, *J. Chem. Phys.* **146**, 134104 (2017), software available at <https://github.com/stochasticHydroTools/RigidMultiblobsWall>.
- [34] S. L. Dance and M. R. Maxey, Incorporation of lubrication effects into the force-coupling method for particulate two-phase flow, *Journal of Computational Physics* **189**, 212 (2003).
- [35] T. Ando, E. Chow, Y. Saad, and J. Skolnick, Krylov subspace methods for computing hydrodynamic interactions in Brownian dynamics simulations, *The Journal of Chemical Physics* **137**, 064106 (2012).
- [36] E. Chow and Y. Saad, Preconditioned Krylov subspace methods for sampling multivariate Gaussian distributions, *SIAM Journal on Scientific Computing* **36**, A588 (2014).
- [37] B. Delmotte and E. E. Keaveny, Simulating Brownian suspensions with fluctuating hydrodynamics, *The Journal of Chemical Physics* **143**, 244109 (2015).
- [38] L. Greengard, Spectral integration and two-point boundary value problems, *SIAM J. Numer. Anal.* **28**, 1071 (1991).
- [39] L. N. Trefethen, *Spectral Methods in MATLAB* (SIAM, 2000).
- [40] R. P. Pelaez, *UAMMD* (2022) <https://github.com/RaulPPelaez/UAMMD>.
- [41] H. Hasimoto, On the periodic fundamental solutions of the Stokes equations and their application to viscous flow past a cubic array of spheres, *J. Fluid Mech* **5**, 317 (1959).
- [42] M. Zuzovsky, P. M. Adler, and H. Brenner, Spatially periodic suspensions of convex particles in linear shear flows. III. Dilute arrays of spheres suspended in Newtonian fluids, *The Physics of Fluids* **26**, 1714 (1983).
- [43] N. Liron and S. Mochon, Stokes flow for a Stokeslet between two parallel flat plates, *J. Eng. Math.* **10**, 287 (1976).